Master's thesis

NTNU
Norwegian University of Science and Technology
Faculty of Natural Sciences
Department of Materials Science and Engineering

Halvor Frøhaug Willumsen

Electrochemical behaviour of Mn-containing Al-alloys after different heat treatment

Master's thesis in Materials Science and Technology
Supervisor: Andreas Erbe
Co-supervisor: Jan Halvor Nordlien
June 2022

NTNU
Norwegian University of
Science and Technology

Halvor Frøhaug Willumsen

Electrochemical behaviour of Mn-containing Al-alloys after different heat treatment

Master's thesis in Materials Science and Technology
Supervisor: Andreas Erbe
Co-supervisor: Jan Halvor Nordlien
June 2022

Norwegian University of Science and Technology
Faculty of Natural Sciences
Department of Materials Science and Engineering

NTNU
Norwegian University of
Science and Technology

Preface

This master's thesis has been written during the spring of 2022 at the Department of Materials Science and Engineering, Norwegian University of Science and Technology (NTNU) as a finalisation of a 5-year master's degree in Materials Science and Engineering. The work is a continuation of a specialisation project on the same topic, conducted by the author during the autumn of 2021. Supervision has been given by Andreas Erbe (NTNU) and Jan Halvor Nordlien at Hydro Karmøy. All experimental work was performed by the author at NTNU, with the exception of ICP-MS analysis which was performed by Anica Simic (NTNU).

Trondheim, June 2022
Halvor Frøhaug Willumsen

Acknowledgements

I would like to thank my supervisor professor Andreas Erbe[1] for helpful guidance and input during the last year. Further, I would like to thank my co-supervisor professor 2 Jan Halvor Nordlien[2] for continued enthusiasm and help, in addition to supplying the aluminium samples. Anita Storsve[1] deserves recognition for lending a helping hand whenever I had problems in the corrosion lab, and Anica Simic[3] for performing the ICP-MS analysis.

[1]Department of Materials Science and Engineering, NTNU, Trondheim
[2]Hydro Aluminium, Karmøy
[3]Department of Chemistry, NTNU, Trondheim

Abstract

Aluminium alloys are frequently used in automotive heat exchangers because of low weight and excellent ability to conduct heat. When the heat exchangers are assembled, they are usually brazed. Heat from the brazing process has been found to activate the aluminium for anodic dissolution processes in aqueous solutions, thus affecting its corrosion resistance. Surface segregation of impurity trace elements like Pb and Sn, present in aluminium alloys, e.g., from recycling and bauxite, are responsible for this activation.

Seven different aluminium alloys, most of which belong to the 3xxx series of aluminium alloys, were studied for their electrochemical properties in acidified synthetic seawater. One alloy containing significantly higher levels of copper was also included. Samples were studied both as-extruded and as-brazed. The surface morphology was characterised by scanning electron microscopy (SEM); elemental composition of selected regions was determined by energy dispersive x-ray spectroscopy (EDS). Surface enrichment of Pb was found by GD-OES during brazing, leading to electrochemical anodic activation. To study the electrochemical behaviour of the alloys in the two conditions, cyclic polarisation scans were performed in the interval -400 mV to +400 mV around the corrosion potential. The polarisation curves collected were additionally used in further development and testing of a machine learning algorithm for predicting polarisation curves based on the alloy composition. Samples of the electrolyte were taken at defined points during these polarisation scans and analysed with inductively coupled plasma mass spectrometry (ICP-MS). For selected samples, the corrosion morphology after polarisation was also studied by SEM.

The aluminium alloy containing Cu was significantly less activated by heat treatment than the other alloys, with a depression of corrosion potential of only 10 mV compared to the as-received sample. Results were inconclusive in determining if Cu reduced surface segregation of Pb, or if the reduced activation was only due to ennoblement of the aluminium. Chemical depth profiles indicated reduced surface segregation, while electrolyte analysis by ICP-MS indicated higher than expected dissolution of Pb. The machine learning algorithm was successful in predicting polarisation curves of alloys which were not part of the training data, however further expansion of the training data is needed for a commercial application of the algorithm to be possible. However, the approach works with experimentally easily accessible amounts of training data and can be used to predict the variation of polarisation curves in alloys with similar base but complex composition.

Sammendrag

Aluminium brukes ofte i varmevekslere i biler på grunn av lav vekt og god varmeledningsevne. Når varmevekslerne monteres blir de ulike delene loddet sammen. Varme fra denne loddeprosessen aktiverer metallet for anodiske oppløsningsprosesser i vandige løsninger, og påvirker derfor korrosjonsmotstanden. Tidligere arbeid har vist at sporelementer som bly og tinn, som er tilstede i aluminium fra for eksempel resirkulering og råstoffet bauksitt, er ansvarlige for denne aktiveringen.

De elektrokjemiske egenskapene i surt syntetisk sjøvann til syv forskjellige aluminiumslegeringer, hvorav flesteparten tilhører 3xxx-serien med aluminiumslegeringer, ble undersøkt. En legering som inneholdt vesentlig høyere mengder kobber ble også inkludert. Prøvene ble undersøkt både som ekstrudert og som loddet. Overflatemorfologien ble karakterisert i SEM, og sammensetningen til utvalgte områder ble karakterisert med EDS. Overflateanrikning av bly ble funnet med GD-OES etter lodding, som ledet til anodisk aktivering. Sykliske polarisasjonsskanninger ble gjennomført for å undersøke de elektrokjemiske egenskapene til legeringene i et område på -400 mV til +400 mV rundt korrosjonspotensialet. De målte polarisasjonskurvene ble i tillegg brukt til videre utvikling av en maskinlæringsalgoritme for å predikere polarisasjonskurver basert på legeringsinnhold. Prøver av elektrolytten ble tatt ved definerte tidspunkt under polarisasjonsforsøkene og analysert med ICP-MS. For utvalgte prøver ble også korrosjonsmorfologien etter polarisering undersøkt i SEM.

Aluminiumslegeringen som inneholdt kobber ble vesentlig mindre aktivert av varmebehandlingen enn de andre legeringene, med en senkning i korrosjonspotensial på kun 10 mV sammenlignet med den som ekstruderte prøven. Resultatene var inkonklusive når det kom til å bestemme hvorvidt kobber reduserte segregering av bly til overflaten, eller om den reduserte aktiveringen kun var på grunn av foredling av overflaten. Kjemiske dybdeprofiler indikerte redusert segregering, mens analyse av elektrolytten med ICP-MS indikerte uventet høy konsentrasjon av bly. Maskinlæringsalgoritmen var i stand til å predikere polarisasjonskurvene til legeringer som ikke var en del av treningssettet, men videre utvidelse av treningsdataene trengs for at algoritmen skal kunne brukes kommersielt. Tilnærmingen fungerer imidlertid med eksperimentelt lett tilgjengelige mengder data, og kan brukes til å predikere variasjonen i polarisasjonskurver i legeringer med lignende grunnlag men kompleks sammensetning.

Contents

List of Tables

List of Figures

Acronyms

EDS Energy-dispersive x-ray spectroscopy.

GD-OES Glow discharge optical emission spectrometer.

HER Hydrogen evolution reaction.

ICP-MS Inductively coupled plasma mass spectrometry.

MAE Mean absolute error.

MPE Multi-port extrusion.

OCP Open circuit potential.

ORR Oxygen reduction reaction.

RF Random Forest.

SEM Scanning electron microscope.

SWAAT Sea water acetic acid test.

List of Symbols

Latin letters

Symbol	Description	Unit
E_{corr}	Corrosion potential	V
E_{pit}	Pitting potential	V
E_{rev}	Reversible potential	V
F	Faraday's constant	C/mol
i_{a}	Anodic current density	$\mathrm{mA/cm^2}$
i_{c}	Cathodic current density	$\mathrm{mA/cm^2}$
i_{corr}	Corrosion current density	$\mathrm{mA/cm^2}$
i_{lim}	Limiting current density	$\mathrm{mA/cm^2}$
i_0	Exchange current density	$\mathrm{mA/cm^2}$
R	Gas constant	J/molK
R^2	Coefficient of determination	-
T	Temperature	K
z	Number of transferred electrons	-

Greek letters

Symbol	Description	Unit
α	Transfer coefficient	-
η	Overpotential	V
η_{act}	Activation overpotential	V
η_{conc}	Concentration overpotential	V

Chapter 1

Introduction

1.1 Background and motivation

The EU aims to reduce its emission of greenhouse gases in line with the Paris Agreement [1]. The low weight of Al allows for reduced emissions from the transport sector by reducing vehicle weight, thus improving fuel efficiency. Furthermore, its excellent ability to conduct heat and electricity makes aluminium useful for a lot of different applications. One of these is the use of aluminium for heat exchangers in cars. Usually, extruded profiles of 3xxx series aluminium alloys are used, and the heat exchangers are assembled by brazing.

In ambient conditions, aluminium is a passive metal, meaning that even though corrosion is thermodynamically favourable, it is prevented due to a passive oxide film protecting the metal [2]. However, when exposed to aggressive conditions, this film may break down so that corrosion occurs. Such conditions exist in the automotive heat exchangers, so good corrosion resistance is paramount in order to avoid service failure. Thus, a lot of work is put into understanding the corrosion behaviour of aluminium in different environments.

One way to evaluate the corrosion properties of a metal is by measuring its polarisation curve. The corrosion current density i_{corr} and corrosion potential E_{corr} can be found from these curves. Figure 1.1 shows a simplified, schematic polarisation curve for an arbitrary corrosion process. E_{corr} and i_{corr} are found at the intersection between the extrapolated anodic and cathodic currents, marked with red lines.

By studying, amongst others, the polarisation curves of heat treated aluminium, it has been found that heat treatment above certain temperatures makes the corrosion properties of wrought aluminium alloys worse. A lot of work has been put into resolving the cause of this behaviour, and it was found that impurity trace elements like Pb and Sn are involved [3, 4]. Certain common alloying elements like Fe and Cu have been found to decrease the effect of the trace elements [5, 6], while Mg have been found to increase the effect of the trace elements [7].

However, the polarisation curves are not always easy to interpret, even for pure metals in controlled environments. Alloying elements further complicates the interpretation. The alloying elements will dissolve at different rates, which means the surface exposed to the electrolyte is constantly changing. The resulting polarisation curves are often very

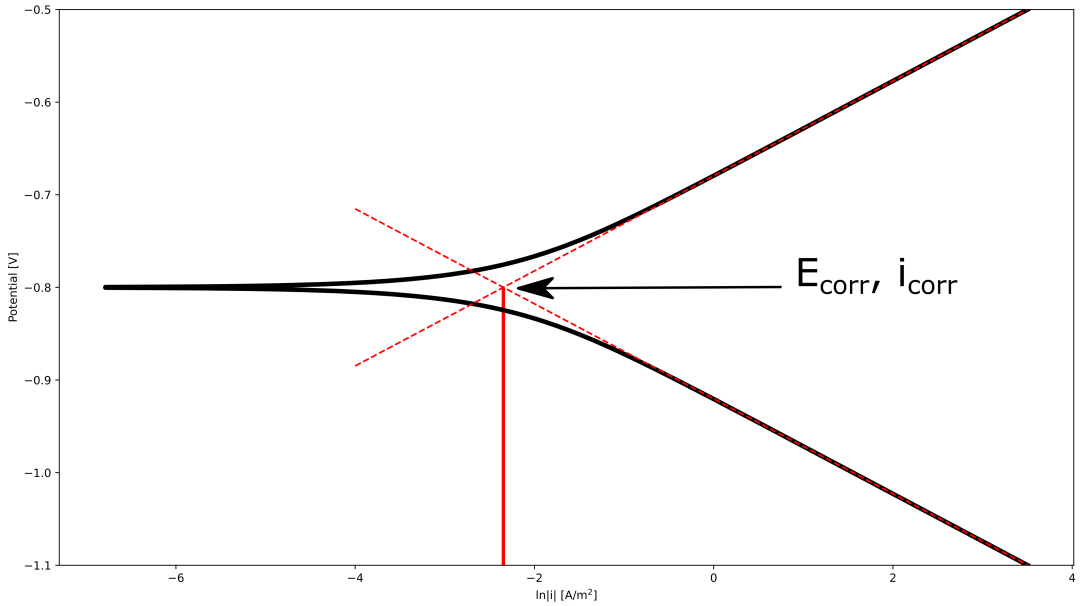

Figure 1.1: E_{corr} and i_{corr} are found at the intersection between the extrapolated currents.

difficult to interpret.

Electrochemical experiments are also time-consuming, and often highly dependent on the experimental environment. As a result, machine learning methods are becoming more popular for studying electrochemistry [8]. This effect is also driven by programming becoming more accessible and easier to use.

1.2 Aim and scope of the work

This work investigates the corrosion behaviour of heat treated commercial multi-port extrusion (MPE) aluminium alloys. The effect of the heat treatment on the corrosion properties will be studied, both by electrochemical methods and by surface and elemental analysis in glow discharge optical emission spectrometer (GD-OES) and scanning electron microscope (SEM) equipped with energy-dispersive x-ray spectroscopy (EDS). A Gamry potentiostat will be used to measure cyclic polarisation scans of the different alloys in acidified synthetic seawater. To supplement this, samples of the electrolyte from the electrochemical measurements taken at different times during the polarisation of the samples will be analysed in inductively coupled plasma mass spectrometry (ICP-MS). The goal of the work is to develop a better understanding of the effect of different alloy elements on the behaviour attributed to Pb and Sn. In addition, the data from the polarisation scans will be used to build a machine learning algorithm for predicting polarisation curves for other alloys. The aim is to discover if machine learning models can be used to predict polarisation curves for aluminium alloys of similar composition, without the need for data collection.

Chapter 2

Theory

2.1 Aluminium

Pure aluminium lacks the strength needed for use in many structural applications such as constructions and cars. The corrosion resistance of pure aluminium is good however. Aluminium forms a protective oxide film which prevents further oxidation of the metal. This oxide film does, however, break down under certain conditions. For example, the solubility of the oxide is high in acidic and alkaline solutions, as shown in Figure 2.1. Likewise, in chloride containing solutions, the oxide film can break down locally. As a result, the corrosion resistance in seawater can be rather poor for some alloys.

To achieve a stronger material, aluminium is alloyed with other metals. Aluminium alloys are commonly divided into series depending on their main alloying elements [9]. The alloying elements strengthen the aluminium in the form of precipitation hardening or solid solution strengthening. Depending on the alloy composition, aluminium alloys will contain different intermetallic particles. As the stoichiometry of these particles differ from the surrounding matrix, there are also commonly differences in electrochemical behaviour [10]. The intermetallic particles can thus make the alloys susceptible to localised types of corrosion such as pitting corrosion. The exact composition of intermetallic particles may vary quite significantly, as equilibrium conditions are seldom obtained during solidification. There can also be significant amounts of alloying elements in supersaturated solid solution.

Alloys in the 3xxx series have manganese as the main alloying element. They are generally low-alloyed and soft. The added manganese forms particles with Al, and other alloying elements or impurities like Si, Fe and Cr. Work hardening can increase the strength of these alloys because of manganese in solid solution.

Mn also increases the corrosion resistance of the alloy by preventing the formation of Fe_3Al-particles. Iron impurities generally form intermetallic particles which act as cathodic sites, decreasing the corrosion resistance [11]. Instead, (Mn, Fe)-Al_6 particles are formed. Mn in solid solution also affects the corrosion potential of the aluminium matrix, the result being that the corrosion potential of particles and matrix are quite similar. Thus, strong microgalvanic coupling is prevented. Still, the alloys are susceptible to pitting in chloride containing electrolytes [12, 13].

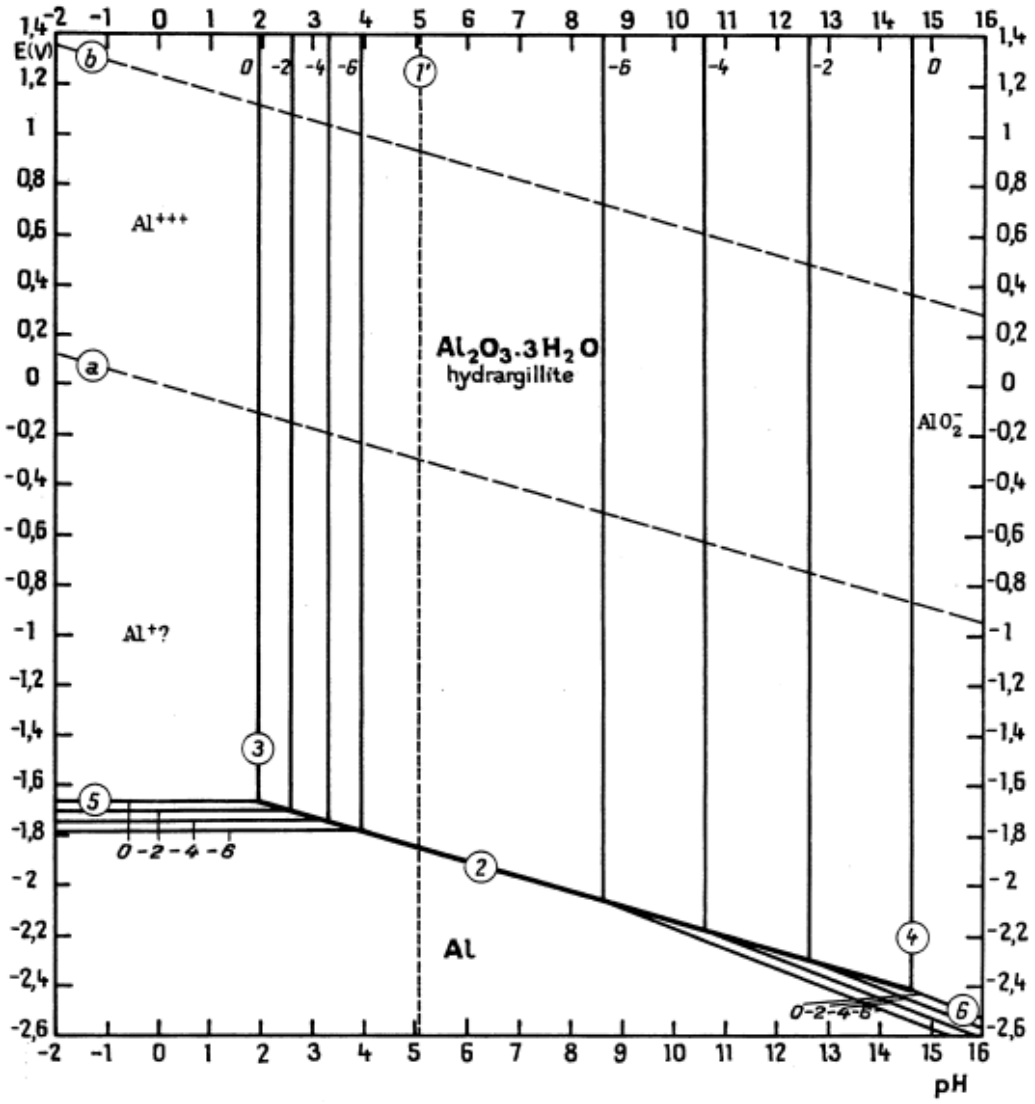

Figure 2.1: Pourbaix diagram for aluminium. The metal is passive between pH 4 and 9 [2]

.

2.2 Corrosion mechanisms in aluminium alloys

Forming intermetallic particles can be more noble or less noble than the aluminium matrix [10]. In both cases, localised corrosion results, as either the particles or the surrounding area are likely to dissolve significantly faster than the remaining part of the surface region. Examples of particles that are more noble include particles like Al_2Cu, Al_3Fe and Al_7Cu_2Fe. Particles which are more active include Mg_2Si, Mg_2Al_3 and $MgZn_2$.

Pitting corrosion is a localised form of corrosion which can cause severe damage by formation of deeply propagating holes. Little is known on the initiation of pitting. However, typical sites for initiation are places where the passivating oxide is weakened [14]. Typical flaws are scratches, cracks or inclusions on the surface. It is widely accepted, with considerable experimental evidence, that chloride ions are adsorbed

$$3Cl^- \longrightarrow 3Cl^-_{ads} \tag{2.1}$$

to the passive oxide film [15, 16]. The chloride then penetrates the oxide film, and a pos-

sible step-wise exchange of oxide or hydroxide with chloride have been hypothesised [17].

$$\mathrm{Al(oxide)OH_2^+Cl_n^{n-}} \rightleftharpoons \mathrm{Al[(nCl-)(oxide)]OH_2^+} \tag{2.2}$$

$$\mathrm{Al[(nCl-)(oxide)]OH_2^+} \rightleftharpoons \mathrm{Al^+[(nCl-)(oxide)]OH_2^+ + e^-} \tag{2.3}$$

$$\mathrm{Al^+[(nCl-)(oxide)]OH_2^+} \rightleftharpoons \mathrm{Al^{2+}[(nCl-)(oxide)]OH_2^+ + e^-} \tag{2.4}$$

$$\mathrm{Al^{2+}[(nCl-)(oxide)]OH_2^+} \rightleftharpoons \mathrm{Al^{3+}[(mCl-)(oxide)]OH_2^+ + (n-m)Cl^- + e^-} \tag{2.5}$$

The dissolved metal can react further with water and chloride to form oxochlorides [18]. After rapid oxidation of the exposed Al, Al^{3+} is hydrolised

$$\mathrm{Al^{3+} + H_2O \longrightarrow Al(OH)^{2+} + H^+}, \tag{2.6}$$

followed by reaction with chloride

$$\mathrm{Al(OH)^{2+} + Cl^- \longrightarrow Al(OH)Cl^+} \tag{2.7}$$

and finally with water, creating acidic conditions

$$\mathrm{Al(OH)Cl^+ + H_2O \longrightarrow Al(OH)_2Cl + H^+}. \tag{2.8}$$

Chloride can also replace water in (2.8), forming $Al(OH)Cl_2$. As H^+ is formed in the reactions, the pH will decrease locally in the pit. Decreasing pH implies higher oxide solubility and thus lower probability of repassivation. Formation of H^+ also causes anions, often dominated by Cl^- to migrate into the pit to neutralise the extra positive charge. The interplay between the aforementioned processes causes a self-accelerated dissolution of a certain region in the material, leading to the formation of pits. The common effect of self-accelerating dissolution and ion migration will continue to cause aggressive conditions inside the pit, which increase the speed of pit propagation. A schematic illustration of the pit propagation process is shown in Figure 2.2.

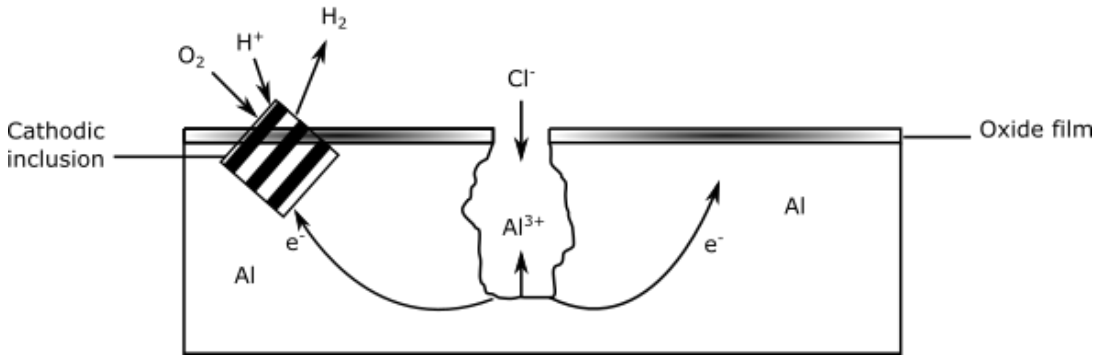

Figure 2.2: Schematic drawing of pit propagation. The cathodic reaction takes place on the cathodic particle on the surface.

2.3 Thermomechanical processing of MPE tubes

In the automotive industry, the 3xxx series are often used as heat exchangers because of their excellent thermal properties. Aluminium alloys used in heat exchanger applications are subject to a series of thermomechanical processing methods. After casting the alloys are usually homogenised followed by extrusion, before the extruded parts are brazed together during assembly of the heat exchangers. A brief introduction to these methods and their effect on the aluminium microstructure is given in this section.

2.3.1 Homogenisation

Before extrusion, the as-cast billets are homogenised. 3xxx series billets are often heated to temperatures up towards 600°C, and held at this temperature for 6 to 12 hours [19]. The purpose of the homogenisation is to create a microstructure that is favourable for extrusion. This includes forming dispersoids that control the grain size during extrusion and distributing alloying elements uniformly in solid solution [20]. In addition, microsegregation and particles causing areas with lower melting temperatures are removed, to avoid surface tearing during extrusion.

2.3.2 Extrusion

Extrusion is a way of processing metal in which a metal bolt is pushed through a die as shown in Figure 2.3. This method is especially suited to produce profiles with complex cross-sections like MPE tubes.

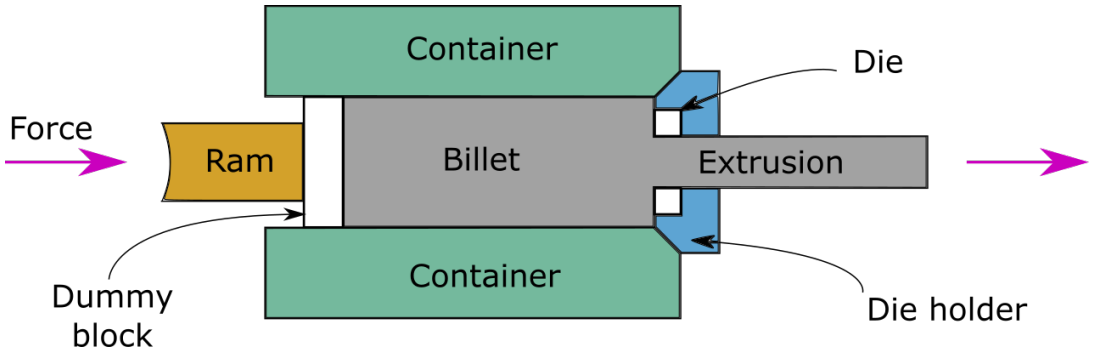

Figure 2.3: Schematic representation of the extrusion process, reproduced from [21]

Low-alloyed aluminium alloys are generally favoured for extrusion, as presence of surface particles can cause surface tearing [22]. Extrusion alters the microstructure of aluminium, and usually grains become elongated. Friction between the aluminium and the die and chamber creates a strain gradient. Because of the strain gradient present, the grains are thinner near the surface than in the centre [23, 24]. This can result in the deformed surface layer having different corrosion properties than the bulk material.

2.3.3 Brazing

Brazing is usually used for producing heat exchangers with complex shapes. The material that will make up the main parts of the heat exchanger is called the core, while the mate-

rial melting to join the different parts together is called clad. The different constituents of a multichannel heat exchanger before brazing is shown in Figure 2.4a.

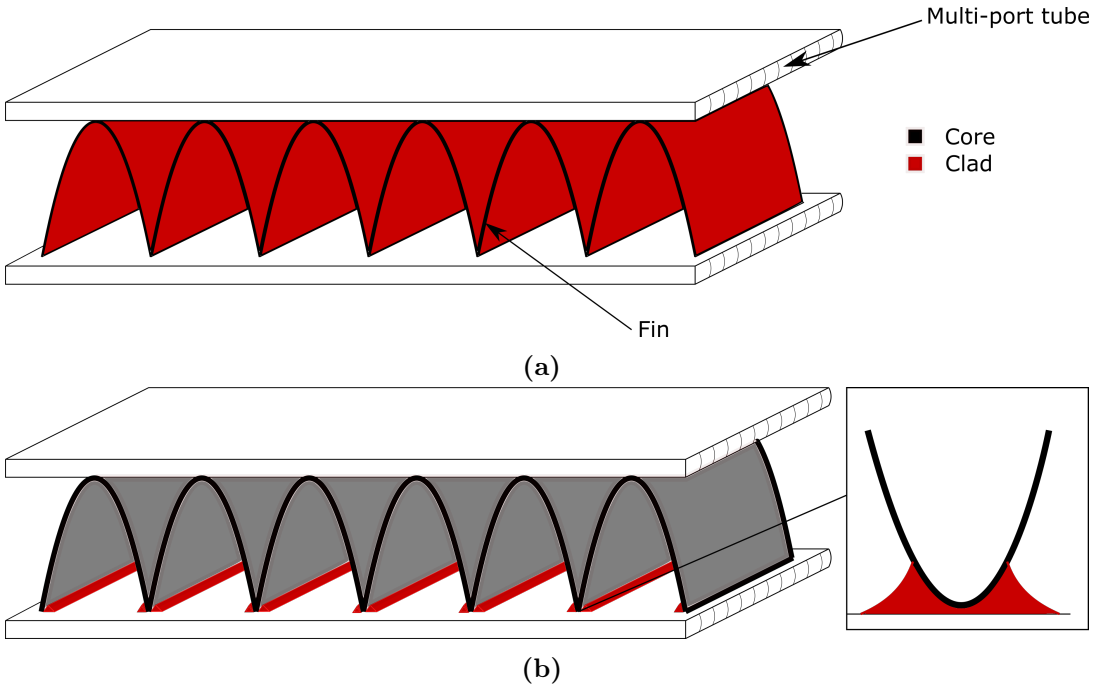

Figure 2.4: **(a)**Before brazing a sandwich structure with core and clad is assembled. **(b)**The clad material has melted and joined the fins and tube together.

When brazed, the core metal is heated to a temperature below its melting point. The cladding material has a lower melting point than the core, and will melt to join the different parts, forming a metallurgical joint as seen in Figure 2.4b. Typically, 4xxx series aluminium alloys are used as cladding material. These alloys contain a high amount of Si, which reduces the melting point of the aluminium [25].

2.4 Effect of brazing heat treatment on electrochemical properties and corrosion

For wrought aluminium alloys the microstructure of the surface differs significantly from the bulk microstructure [26, 27]. Hot-rolling or extrusion imposes high shear on the surface, often in contact with oxygen at high temperatures. As such, the elemental composition and structure of the surface has a huge impact on the corrosion properties of the material.

The heat from the brazing treatment changes the microstructure of the aluminium alloys. Heat causes diffusion of different alloying and trace elements within the alloy. Trace elements in the IIIA-VA groups have been of particular interest in previous work, and their effect on the electrochemical properties of Al has been studied extensively in this laboratory [28, 29, 30].

Work by Afseth et al. [3] showed a negative shift in E_{corr} in a commercial AA3005 alloy as result of heat treatment. The negative transient was the highest for the sample annealed

for 2 h at 500 ° C, where the measured potential was 200 mV lower than the as-received sample.

Further work by the same group investigated the effect of trace elements in the IIIA-VA groups. Heat treatment caused an enrichment of these elements in the alloy surface, causing anodic activation of aluminium in chloride containing solutions [28, 31, 32]. When the aluminium is anodically activated, the pitting potential is significantly depressed. There is also an increase in the anodic current at potentials where Al should be passive. The effect of anodic activation is illustrated in Figure 2.5.

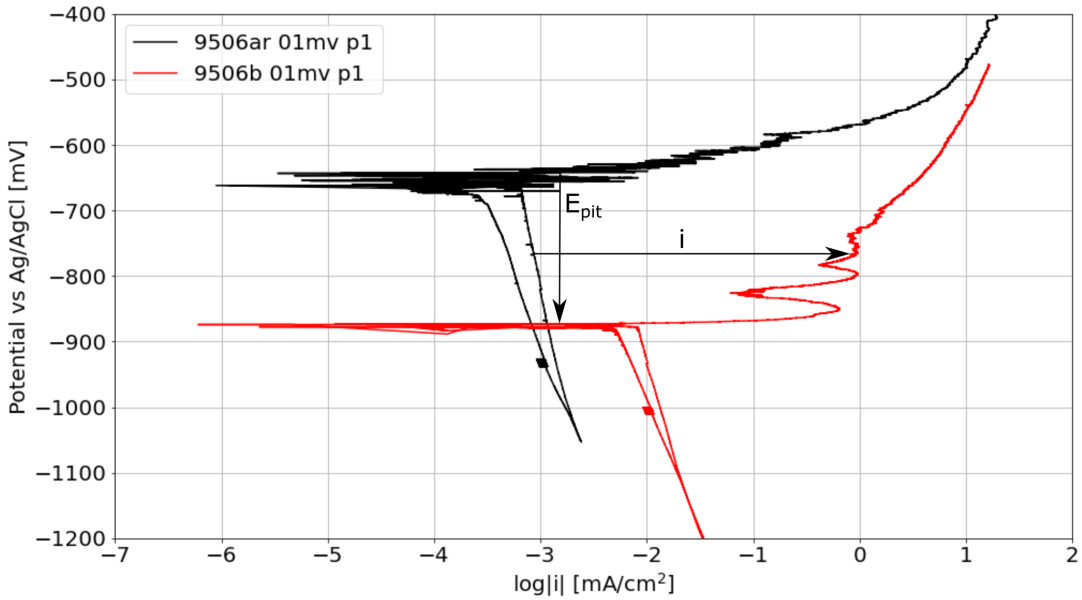

Figure 2.5: Polarisation curves for the two conditions of the 9506 alloy as measured in this work at a sweep rate of 0.1 mV/s in acidified synthetic sea water. The arrows indicate the increase in anodic current density and decrease in pitting potential of the brazed specimen relative to the as-extruded specimen [4].

The classical model of a Hg drop wetting the aluminium surface have been found suitable to explain the mechanism of activation by many of the group IIIA-VA trace elements [4]. The Hg drop prevents repair of the protective oxide film, causing aluminium to dissolve into the drop and form an amalgam.

Table 2.1: Properties of selected activating trace elements in aluminium [33, 34, 35, 36, 37].

Element	**Al**	**Pb**	**Sn**	**In**	**Ga**
Melting point [°C]	660	327	232	157	30
Maximum solubility [wt%]	-	0.20	0.10	0.19	20
Temperature of max sol. [°C]	-	658	625	639	26.6

Pb, In and Sn segregate as nanoparticles as a result of thermomechanical processing because of their low solubility in aluminium. It is well known that the melting point of a particle changes when its size decreases towards the atomic scale [38]. If a particle has free surfaces within the surrounding matrix, it is called a free particle. Such particles experience a depression in their melting point [39]. Coherent particles on the other hand

have a one to one match with the surrounding matrix, meaning that they have no free surfaces. The depression in melting point is important both because it influences diffusion and because it makes the Hg drop model more feasible for the elements in question.

2.4.1 Effect of lead

Because it is present in the bauxite ore, Pb is a common trace element in aluminium alloys [40]. As shown in Table 2.1, Pb has very low solid solubility in aluminium. A maximum of 0.2 wt% is reached at 658 °C [34]. The low solubility in combination with high mobility at the brazing temperatures leads to accumulation of Pb near the aluminium surface.

Pb forms a continuous or near continuous film of nanometer scale thickness between the $\gamma - Al_2O_3$ and the aluminium matrix [41]. A saturation level of Pb in the nanofilm was reached. This means that the degree of anodic activation is not influenced by the concentration of Pb in the bulk [42]. Metallic Pb nanoparticles are also formed, however they are not causing anodic activation. Pb become available on the metal-oxide interface by selective dissolution of aluminium, which reduces the passivity of the oxide film. The enrichment of lead on the surface was also found to promote galvanic corrosion while mitigating pitting corrosion [28].

A common trait for aluminium alloys activated by Pb is the appearance of two oxidation peaks in the anodic branch of the polarisation curve. Anawati et al. attributed the oxidation peaks to destabilisation of the oxide layer followed by crevice corrosion [30, 43].

Enrichment of Pb was found to be the cause of the activation when the model alloys were heat treated at 600 °C [42], however it could not explain activation when the alloys were heat treated at 300°C. Segregation of Pb is insignificant at this temperature. As 300 °C is below the melting point of Pb, diffusion of Pb is dependant on the mobility of Pb in solid solution which is low [44]. At the lower annealing temperatures, other trace elements were responsible for the anodic activation.

2.4.2 Effect of In

In relation to the work with Pb, the same group studied the effect of In on anodic activation. It was shown that In segregated to the surface most effectively and activated the aluminium model alloy when heat treated at 300 °C [45]. After annealing, blisters and pits were observed on the model alloys. EDS analysis of the blister cross-section indicated that the blisters consisted of aluminium oxide, with no detectable amount of In [29]. It was suggested that the blisters were caused by heat treatment making surface In diffuse into the aluminium substrate. The effect of the blisters on the electrochemical properties of the model alloy was not determined.

2.4.3 Effect of Sn

Presence of Sn in aluminium alloys comes mainly from recycling. Like Pb, Sn also has a low solid solubility in aluminium. A maximum of 0.12 wt% can be solved at 600 °C [35]. Tan et al. [40] showed that, like for In, segregation of Sn was the highest for model alloys annealed at 300 °C. Model alloys with up to 500 ppm Sn was only activated after heat treatment at 300 °C, however, a model alloy with 1000 ppm Sn was activated even

without heating [4]. Sn segregated both as nanoparticles and in the form of nanoscale enrichment along selected crystallographic planes [46]. Compared to Pb and In, Sn was the most effective activator. This is indicated by both a larger anodic current and a more significant decrease in pitting potential under identical conditions. Furthermore, Sn segregated as nanoparticles activated the aluminium, contrary to what was found for Pb.

2.4.4 Synergistic effects from multiple trace elements

The presence of two or more Group IIIA-VA elements together can activate the aluminium more than what is expected from the single element alone. For example, synergistic effects occur for the combination of Ga-Sn [47] and Pb-Sn [48].

Unlike the trace elements mentioned in the previous sections, Ga has a high solubility in aluminium. In the case of Ga-Sn, the aluminium was activated even without the presence of chloride. Further studies found that the presence of Ga together with Pb could cause anodic activation, however Ga without Pb had limited effect [49]. When Pb was present Ga were found to segregate by dealloying around lead particles, forming an amalgam with aluminium.

2.4.5 Interplay with alloying elements

In commercial alloys, the effect of trace elements can be enhanced or mitigated by alloying elements. Mg has been shown to promote segregation of Pb by formation of spinel $MgAl_2O_4$ [7]. At 450 °C, Mg increased the activation of an Al-Mg-Pb model alloy compared to an Al-Pb alloy. However, at 600 °C the spinel $MgAl_2O_4$ had a passivating effect causing the Al-Mg-Pb alloy to become less activated than the model Al-Pb alloy.

Presence of alloy elements more noble than Al, such as Si, Mn, Cu and Fe counteracts anodic activation when in solid solution [50]. This effect was less significant for the less noble elements Fe, Mn and Si. Alloying with 0.5 wt% Cu reduced the anodic activation by Pb significantly. Two mechanisms causing this effect was suggested. Firstly, adsorption of Pb on Cu by underpotential deposition was thought to reduce the surface mobility of Pb, hindering destruction of the passive oxide. A requirement for this is enrichment of Cu on the surface. Secondly, the reduced activation was hypothesized to be due to Cu contracting the aluminium lattice, resulting in less Pb in solid solution in the near surface sublayer [5]. However, Anawati et al. [6] later showed that the Pb nanofilm was still formed in a ternary AlPbCu alloy containing 20 ppm Pb and 0.5 wt% Cu. The reduced activation was thus attributed to ennoblement of the aluminium by Cu in solid solution.

2.5 Polarisation curves

When aluminium corrodes, the general oxidation reaction occurring can be described as

$$\mathrm{Al} \longrightarrow \mathrm{Al}^{3+} + 3\mathrm{e}^{-}. \tag{2.9}$$

Another mechanism of aluminium oxidation is the formation of oxides and hydroxides,

$$2\mathrm{Al} + 3\mathrm{H_2O} \longrightarrow \mathrm{Al_2O_3} + 6\mathrm{e}^{-} + 6\mathrm{H}^{+} \tag{2.10}$$

and

$$\mathrm{Al} + 3\mathrm{OH}^- \longrightarrow \mathrm{Al(OH)_3} + 3\mathrm{e}^-. \tag{2.11}$$

In aqueous solutions the corresponding reduction reaction taking place is often either the oxygen reduction reaction

$$\mathrm{O_2} + 4\mathrm{H}^+ + 4\mathrm{e}^- \longrightarrow 2\mathrm{H_2O}, \tag{2.12}$$

or the hydrogen evolution reaction

$$2\mathrm{H}^+ + 2\mathrm{e}^- \longrightarrow \mathrm{H_2}. \tag{2.13}$$

The rate at which the reactions occur are related to the potential of the reaction via the Butler-Volmer equation [51]. For cathodic reactions, the current can be expressed as

$$i_\mathrm{c} = i_0 \exp\left(\frac{-\alpha z F \eta_{\mathrm{act,\ c}}}{RT}\right), \tag{2.14}$$

where i_0 is the exchange current density, α is the transfer coefficient, z is the number of electrons transferred, F is Faraday's constant, R is the gas constant, T is the temperature in Kelvin and $\eta_{act} = E - E_\mathrm{rev}$. Similarly, for anodic reactions, the relation becomes

$$i_\mathrm{a} = i_0 \exp\left(\frac{(1-\alpha) z F \eta_{\mathrm{act,\ a}}}{RT}\right). \tag{2.15}$$

Plotting the logarithm of the sum of the anodic and cathodic currents against the electrode potential yields the polarisation curve shown in Figure 2.6. Here, α is 0.5 and E_rev is set to -0.8 V.

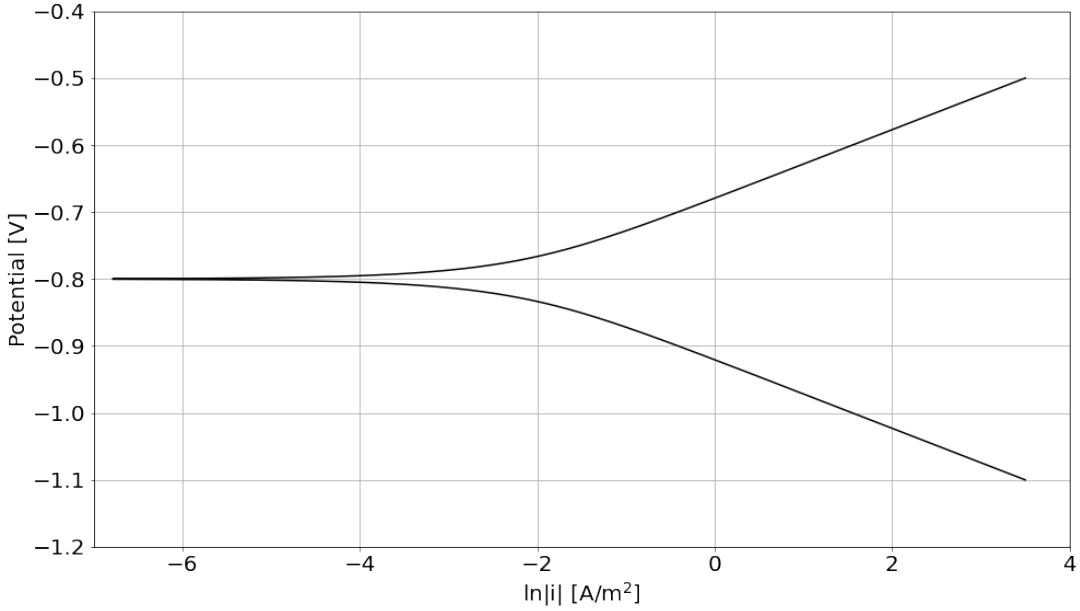

Figure 2.6: Simple polarisation curve based on Equation 2.14 and (2.15)

Depending on the environment in the cell, concentration polarisation can also occur. The polarisation occurs due to the passage of current through the electrolyte. Enrichment of dissolved species near the reactive surface and the build up of a concentration gradient

leads to a slow down of the dissolution process. Dissolution of metal happens faster than the dissolved species diffuse away from the surface, and we get a transition to a diffusion limited scheme. This will cause the anodic branch to curve. On the cathode, the transport of oxygen to the electrode might be limiting. The current from this process can be described as

$$i_{\mathrm{c}} = i_{\mathrm{lim,\ c}} \left(1 - \exp(\frac{zF\eta_{\mathrm{conc,\ c}}}{RT})\right), \tag{2.16}$$

where η_{conc} now is the concentration overpotential and $i_{\mathrm{lim,\ c}}$ is the cathodic limiting current density. Reformulating (2.14) and (2.16), they can be added to give an approximate value for the total cathodic current density:

$$i_{\mathrm{c,\ tot}} = \frac{i_0 \exp(-\alpha zF\eta/RT)}{1 + \frac{i_0}{i_{\mathrm{lim,\ c}}} \exp(-\alpha zF\eta/RT)}. \tag{2.17}$$

Using the same relation for the anodic current, the total current can be expressed as

$$i_{\mathrm{tot}} = i_{\mathrm{c,\ tot}} + i_{\mathrm{a,\ tot}} = \frac{i_0 \exp(-\alpha zF\eta/RT)}{1 + \frac{i_0}{i_{\mathrm{lim,\ c}}} \exp(-\alpha zF\eta/RT)} + \frac{i_0 \exp((1-\alpha) zF\eta/RT)}{1 + \frac{i_0}{i_{\mathrm{lim,\ a}}} \exp((1-\alpha) zF\eta/RT)}, \tag{2.18}$$

where $i_{\mathrm{lim,\ a}}$ is the anodic limiting current. Taken the anodic and cathodic limiting currents into account, Figure 2.6 will transform to Figure 2.7. The curve becomes asymmetrical since the anodic limiting current is set to a larger value than the cathodic limiting current.

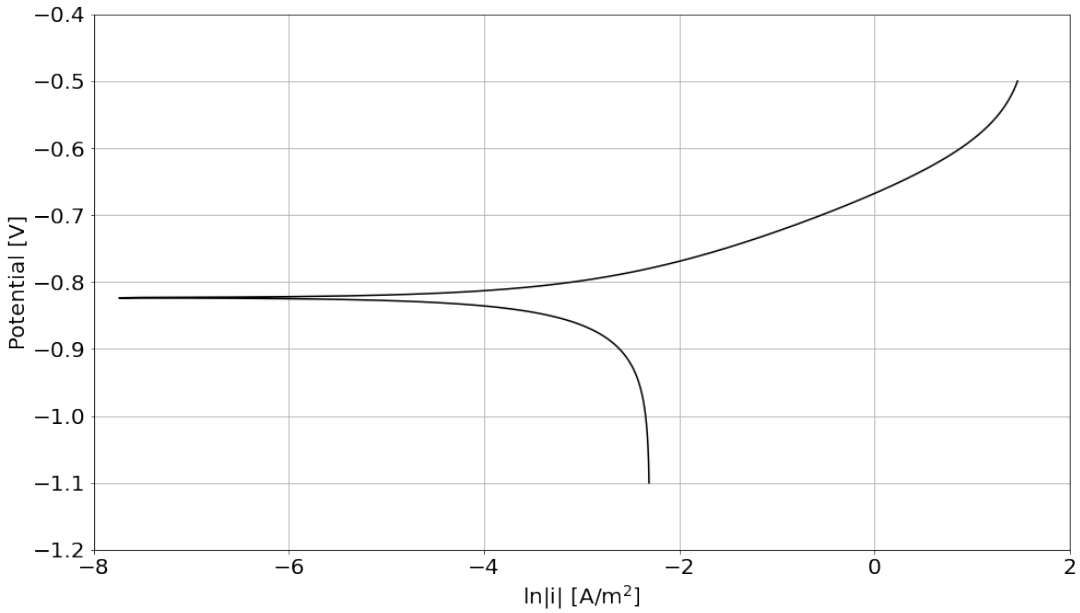

Figure 2.7: Polarisation curve for a thought corrosion process with limiting currents taken into account.

The current recorded at each applied potential will be the sum of the cathodic and anodic currents. Extracting E_{corr} and i_{corr} directly is therefore not necessarily easy [52]. If both the hydrogen evolution reaction (HER)(2.13) and the oxygen reduction reaction (ORR)

(2.12) occurs, the cathodic branch will be further complicated. Similarly, the anodic branch will be affected when dealing with alloys [53]. Not only will the alloying elements affect the anodic part of the curve; they will also influence the cathodic branch. The rates at which the HER and ORR occurs will depend on the metal surface they occur on [54]. For aluminium and many other metals, the passive film on the surface will also play a part. The potential where breakdown of this film starts, E_{pit}, is often marked by a sharp edge in the polarisation curve as shown in Figure 2.8.

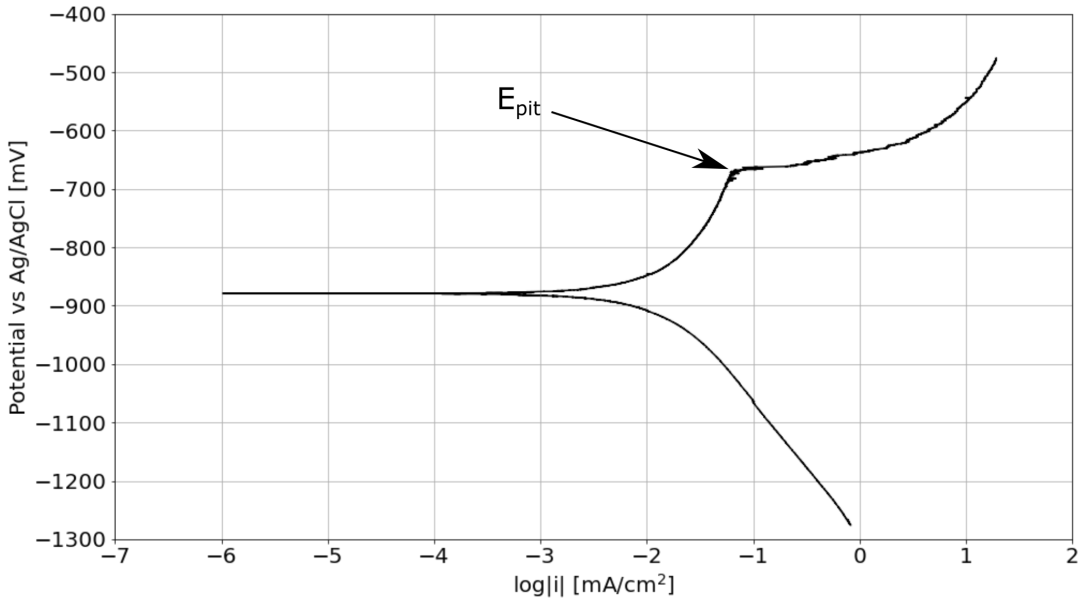

Figure 2.8: Pitting potential for the polarisation scan of the 9520 alloy in the brazed condition measured in this work.

The consequence of all the factors discussed in this section is that a complete mathematical model to describe all features in the polarisation curves is impossible at the present level of understanding. Thus, alternate methods to describe and interpret the curves become a subject of interest. One such method is machine learning, which will be discussed briefly in the next section.

2.6 Machine learning

Machine learning methods for studying corrosion have become popular in recent years. With advanced algorithms becoming available for the general public, machine learning can be used even without much programming experience. In its simplest form, the machine learning algorithms are given a set of input *features* and their related solutions. For predicting polarisation curves, these features could be e.g. alloy composition and electrode potential as is the case in Table 2.2.

A popular machine learning algorithm is the random forest (RF) algorithm. The algorithm has excellent predictive powers, and require little data preparation. However, there is still the risk of overfitting. As averaging is a big part of the algorithm, it is also not very well suited for predicting values outside the available data (i.e. the training set).

Much of the work conducted related to machine learning and corrosion has been focused on parameters related to the electrolyte in which corrosion occurs. For example, Gong

Table 2.2: An example feature matrix with the corresponding solution.

Input				Output
E	**Si**	**Fe**	**Mn**	**i**
$E_{t=0}$	0.12	0.20	0.7	$i_{t=0}$

et al. [55] used different machine learning algorithms to predict polarisation curves of copper in aqueous solution with varying chloride and sulphide concentrations. Among the algorithms tested, they found that the RF algorithm had the best predictive accuracy. Another study focused on the effect of corrosion inhibitors [56], concluding that the RF algorithm was well suited for predicting corrosion rate in presence of inhibitors.

Some work have also been done with alloy composition as input data, but usually with a rather simple output. For example, a study on corrosion rates of different low-alloyed steels was done by Diao et al. [57]. In their prediction model, they used the alloy composition as input parameters . Improved predictive accuracy when tailoring new input parameters based on thermodynamic properties was also demonstrated.

However, polarisation curves of metals with varying alloy composition has not yet been predicted with machine learning. A reason for this is the complex nature of the alloy composition. One would likely need to vary the alloying elements systematically, and one would also need a multitude of different alloys. Compared to the study of corrosion rates, the polarisation curves contain a lot more rows of data. As a consequence of this, the computation time is a lot longer. In some way, this also limits the amount of different parameters that is reasonable to give to the algorithm. The more parameters, the more the computation time will increase.

Chapter 3

Experimental

3.1 Samples

Norsk Hydro ASA provided nine different extruded aluminium alloys for use in this work. All alloys were delivered both as-received (extruded) and as-brazed (extruded and heat treated). The as-brazed samples were heat treated according to Figure 3.1 in a commercial brazing oven.

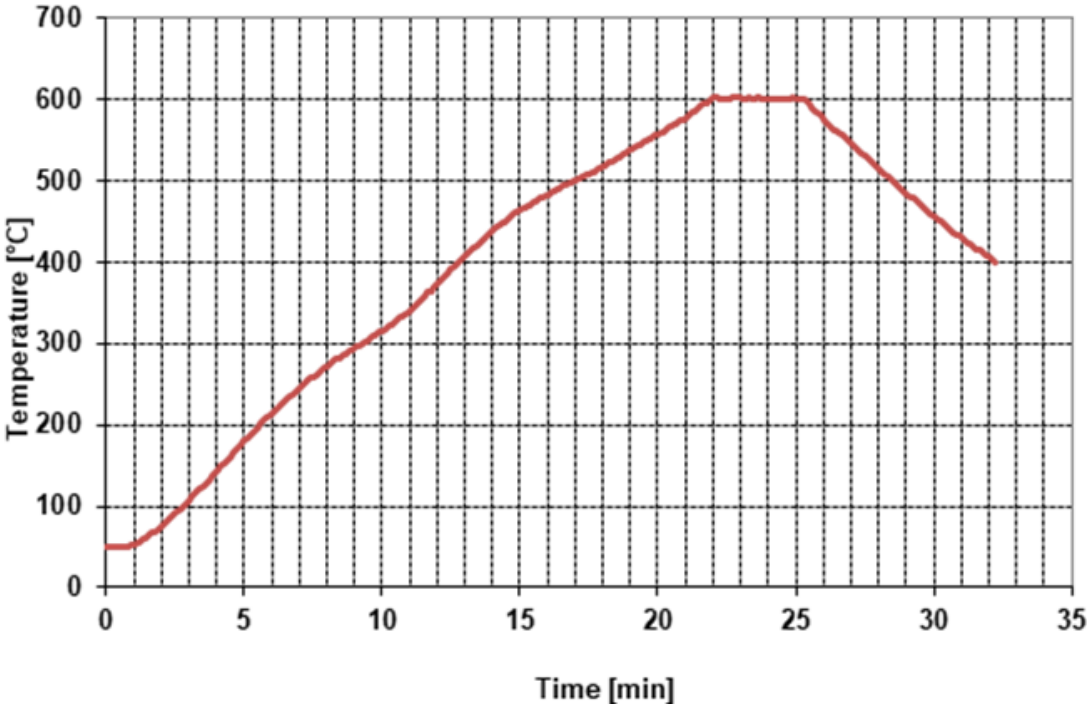

Figure 3.1: Brazing cycle for MPE tubes as brazed by Norsk Hydro ASA.

The chemical composition of the alloys used in this work are shown in Table 3.1. For further convenience, the as-brazed and as-received samples are denoted with the suffixes b and ar, respectively.

Table 3.1: Alloy composition in wt%.

Alloy	Si	Fe	Cu	Mn	Mg	Cr	Ni	Ti	Zn	Others tot
1197	0.08	0.15	0.44	0.15	-	-	0.01	0.02	-	-
9108	0.12	0.20	-	0.70	0.01	-	-	0.01	-	-
9170	0.06	0.10	-	0.43	-	0.07	-	0.02	-	-
9170gc	0.04	0.10	-	0.43	-	0.06	-	0.01	-	-
9506	0.26	0.16	-	0.58	0.01	0.11	0.01	0.04	0.01	0.10
9507	0.07	0.13	-	0.29	-	0.09	0.01	0.03	0.01	0.10
9509	0.07	0.10	-	0.56	0.01	-	0.01	0.01	-	0.10
9510	0.18	0.17	-	0.60	0.01	0.13	-	0.13	-	-
9520	0.07	0.09	-	0.16	-	0.12	-	0.14	-	0.10

3.2 Electrochemical Experiments

Acidified synthetic seawater was used as the electrolyte in all the experiments. This electrolyte is similar to the solution used in the sea water acetic acid test (SWAAT), which is frequently used for corrosion testing in the industry. The electrolyte was prepared based on ASTM D1141 [58], with minor modifications; compounds with concentration less than 0.5 g/L were neglected, and the solution was prepared by dissolving the salts in ion free distilled water. The chemical composition of the modified synthetic seawater is shown in Table 3.2. After dissolving the salts, the pH was adjusted to 2.8-3.0 using concentrated, 99.8% acetic acid. The pH was measured using a pH electrode.

Table 3.2: Ion content in synthetic seawater as used in this work.

Compound	Concentration [g/L]
NaCl	24.53
$MgCl_2$	5.20
Na_2SO_4	4.09
$CaCl_2$	1.16
KCl	0.695

To remove any dissolved oxygen, the electrolyte was purged with nitrogen gas for 5 minutes before any measurements were performed. After purging, a nitrogen atmosphere was maintained over the electrolyte. Each sample was then subject to a series of experiments, as shown in Figure 3.2. All experiments were conducted using a Gamry potentiostat. For the cyclic polarisation scans the Gamry potentiostat sweeps across a potential range. The current required to obtain each potential is measured [59]. A Ag/AgCl electrode in saturated KCl was used as the reference electrode, while the counter electrode was Pt.

The series of electrochemical experiments were done at a scan rate of 0.1 mV/s. A sample holder with opening diameter 8.85 mm was used for all the experiments. The surface area of the sample exposed to the electrolyte was 0.62 cm^2. For each cyclic polarisation scan the sample was first polarised 400 mV in the cathodic direction. From there, the sample was polarised 800 mV in the anodic direction.

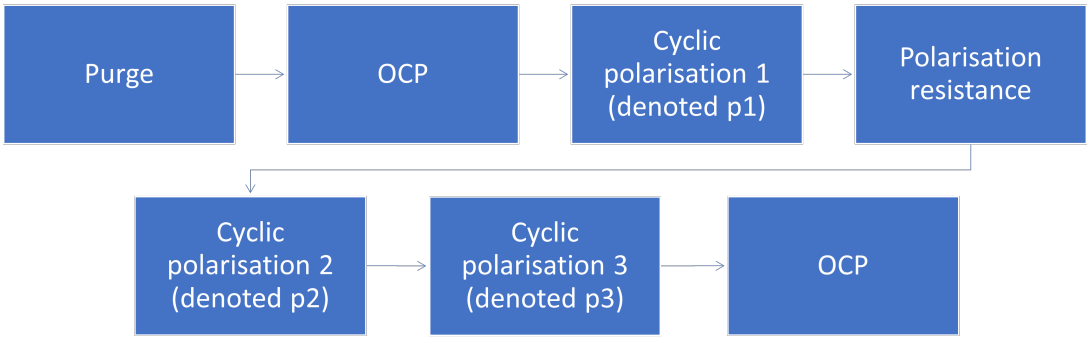

Figure 3.2: Flowchart showing the series of electrochemical experiments.

3.3 SEM

The surface morphology was studied in SEM both before and after polarisation. In addition, elemental analysis were performed using EDS. All EDS spectra were collected with an acceleration voltage of 15 kV. The aperture radius was 30 µm, and the collection time was 30 s. A Zeiss Supra 55 VP was used for all the SEM and EDS experiments.

3.4 GD-OES

Chemical depth profiles for the samples were recorded with a Horiba Scientific GD-Profiler 2. Each sample was sputtered with an Argon plasma source, and the sputtered area was approximately 5.27 mm^2. The content of each element were quantified to wt% by calibrating the instrument with aluminium samples of known composition. The parameters used are summarised in Table 3.3.

Table 3.3: Parameters used for the GD-OES analysis.

Parameter	**Value**
Flushing Time	90 s
Preintegration time	100 s
Background	5 s
Measurement time	120 s
Pressure	600 Pa
Power	32 W
Module	7 V
Phase	4 V

3.5 ICP-MS

Samples of the electrolyte were taken during polarisation of the samples 1197ar, 1997b, 9506ar and 9506b. For all four alloy samples, electrolyte samples were taken after cathodic polarisation and halfway through the anodic polarisation. This corresponded to the

potentials E_{corr} and E_{corr} + 150-200 mV for all alloys. Due to limited availability to the ICP-MS instrument, the electrolyte samples were stored in glass containers in a cabinet for two months while waiting for analysis.

Before analysis, all samples were diluted 100 times with 0.1 M HNO_3. To keep track of the exact dilution factor, sample containers were weighed empty, with HNO_3 and finally with the added electrolyte sample. The concentration of Al, Cr, Cu, Fe, Mn, Pb and Si were analysed in all samples. The samples were analysed on an Agilent 8800 QQQ, equipped with a prepFAST M5 autosampler using hydrogen/helium and oxygen/helium gases mixtures in MS/MS mode.

The total charge experienced for each sample was calculated by integration of the measured current with respect to time,

$$Q = \int_{t_{\text{corr}}}^{t_{\text{sample}}} I(t)dt. \tag{3.1}$$

Equation 3.1 was approximated by using the trapezoidal rule. t_{corr} represents the time when the potential returns to E_{corr} after cathodic polarisation, and t_{sample} is the time elapsed when the potential reached E_{corr} + 200 mV and the second electrolyte sample was taken. The calculated charge was then converted to corroded mass

$$m = M\frac{Q}{zF}, \tag{3.2}$$

where M is the molar mass, z is the number of electrons transferred in the oxidation reaction and F is Faraday's constant. By assuming uniform dissolution, the expected concentration of each alloy element was calculated by multiplying Equation 3.2 with the content of each element in the alloy.

3.6 Data-based modelling

Parts of this section is based on previous work by the author, in which the main part of the work related to machine learning was done [60].

The programming language Python was used for machine learning. Results from other comparison studies showed that the RF algorithm is well suited for electrochemical experiments [55, 56]. With this in mind, the RF algorithm was chosen as the main algorithm for this work. The built-in RF Regressor in the scikit-learn library was used to build the machine learning model [61]. To ensure reproducibility, the model was given the seed 1234. *n_estimators* was set to 500, as no real improvement of the predictive accuracy was seen for values larger than this. At the same time, the data set was small enough for the algorithm to run in reasonable time with this many estimators. For the same reason, the *max_depth* parameter deciding the maximum number of splits before the terminal node is reached was set to the default *None*. This means that the algorithm will run until all nodes are pure and no further variance reduction is possible.

3.6.1 Filtering and sampling

To remove data outliers and noise, the input data was run through a filter in Python. The filter was only applied on potentials more than 100 mV below the open circuit potential

(OCP), to ensure that no actual features were removed from the data set. For each data point run through the filter, the code would check if there was a great difference between the current density in this point and the next. This threshold difference was set to 10^{-6} mA/cm^2. If the points fulfilled this criterion, the first point was set equal to the second point. Figure 3.3b shows the filtered version of the polarisation curve in Figure 3.3a.

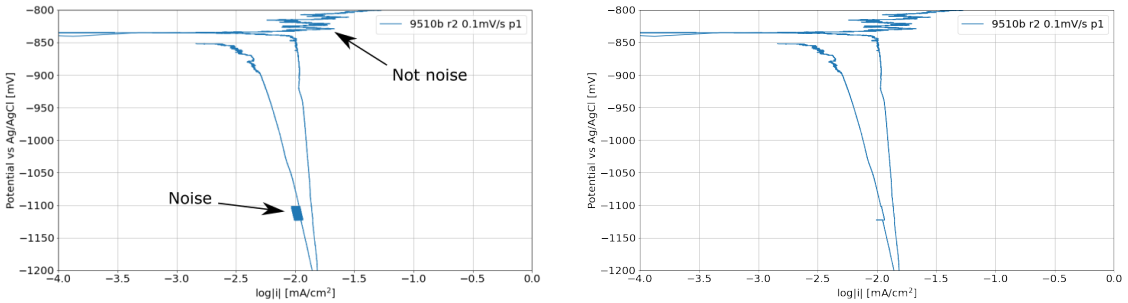

(a) **(b)**

Figure 3.3: The polarisation curve in a) is filtered, yielding the curve in b).

When dealing with great amounts of data, correct sampling becomes important to reduce the computation time. Sampling the data of polarisation curves is not a straight-forward task however. Each area of the polarisation curve is of different importance. The area close to E_{corr} contains fewer data points and should be sampled with care compared to the anodic and cathodic ends of the curve. This means one cannot just sample the data uniformly. An algorithm was developed to handle this problem. For each polarisation curve, the algorithm identified E_{corr} by identifying areas with rapid change in measured current. In a potential range within $\pm$ 25 mV of E_{corr}, all data points were included. Outside this "grace area", every fifth point was sampled. This reduced the amount of data points for each curve by about 45000. A visual representation of the sampling algorithm is shown in Figure 3.4.

3.6.2 Feature selection

In addition to sampling, being conservative with the amount of input features can also increase the speed of the algorithm. To make the training faster, alloying elements with a concentration below 0.01 wt% in both alloys were excluded from the input data. Some of the measured currents are many orders of magnitude lower than the electrode potential. To reduce the difference in magnitude between the parameters, all current densities were multiplied by 1000.

For each test of the algorithm, one of the data sets from Table 3.4 was kept out of the training data. This data set was then used to validate the model. In total, the polarisation data for 7 different alloys were used in each iteration. The 1197 alloy was initially kept out of the input data sets, as it was the only alloy containing appreciable amounts of Cu. Predictive accuracy was therefore decreased when the 1197 data was included. However, a modified version of the model was adapted to include and predict the 1197 curves. Table 3.4 gives an overview of the data used to build the model for the brazed samples, with nomenclature as given in Figure 3.2. For the modified version of the model, the input features Mg, Ti and Cr were replaced by Cu content. In addition,

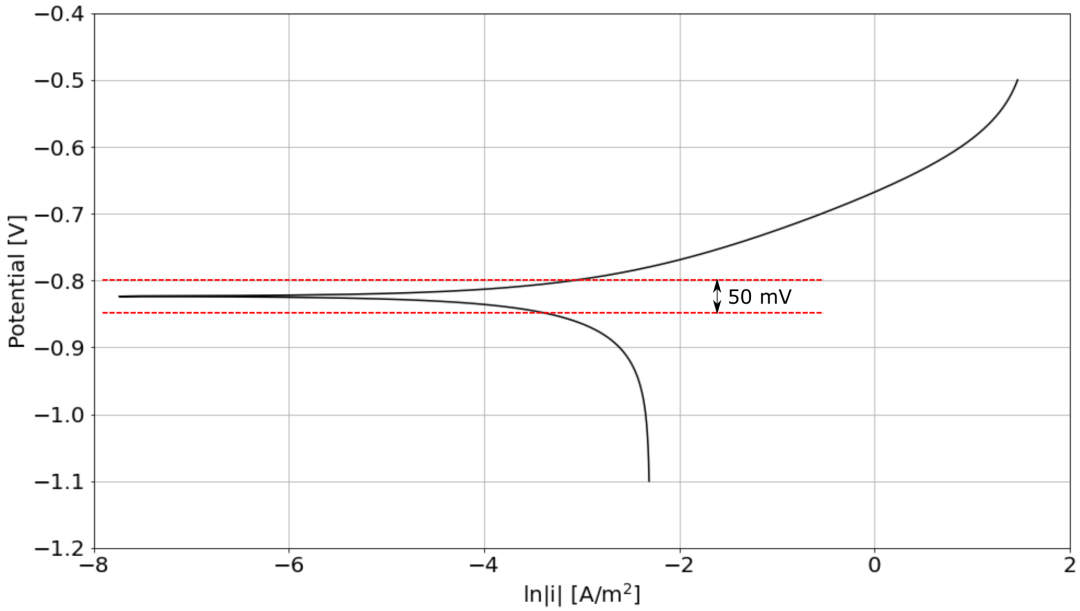

Figure 3.4: Visual representation of the tailored sampling algorithm. Inside the dashed red lines, every point is included. Outside this 50 mV "grace" area, every fifth point is included.

data for the 1197 alloy was added to the data in Table 3.4. The same approach was used for the as-extruded samples.

Table 3.4: Data sets used to build the machine learning model for the brazed samples. Samples marked with * are data from previous work by the author[60].

Sample	p1	p2	p3
9108b r1*	x	x	x
9108b r2*	x	x	x
9170b r1	x	x	x
9170gcb r1	x	x	x
9506b r1	x	x	x
9507b r2	x	x	x
9509b r1	x	x	x
9510b r1*	x	x	x
9510b r2*	x	x	x
9520b r1	x	x	x

Using the knowledge that the as-brazed samples contain a surface layer that is undermined after one round of polarisation, measures were taken to discern between the first and non-first polarisation scans. The easiest way to account for this is to add a binary variable keeping track of the scan's place in the sequence. A column with ones and zeros was added to the feature matrix. The rows containing data from a first scan will have the number one in this column, while data from the second and third scans will have a zero. Table 3.5 shows a schematic representation of the feature matrix and the target vector.

Table 3.5: Illustration of the input feature matrix and the output target vector given to the machine learning model for the brazed samples. For each test of the model, one alloy data set from Table 3.4 was kept out of the input data.

Input								**Output**
E	**First (1/0)**	**Si**	**Fe**	**Mn**	**Mg**	**Ti**	**Cr**	***i***
E(t=0s) 9108b r1 p1	1	0.12	0.20	0.7	0.010	0.01	0	i(t=0s) 9108b r1 p1
⋮	⋮	⋮	⋮	⋮	⋮	⋮	⋮	⋮
E(t=6000s) 9506b p2	0	0.26	0.16	0.58	0.01	0.11	0.04	i(t=6000s) 9506b p2
⋮	⋮	⋮	⋮	⋮	⋮	⋮	⋮	⋮
E(t=12000s) 9520b p3	0	0.07	0.09	0.16	0	0.12	0.14	i(t=12000s) 9520b p3

3.6.3 Performance assessment

In addition to visual assessment, built-in functions in the RF Regressor were used to evaluate the performance of the machine learning model. The *score* function was used to evaluate the predictive accuracy of the model by calculating the coefficient of determination R^2, while the *feature_ importance* function was used to analyse the weighting of each feature in the model. The code written to produce the results in this work is attached in Appendix C.

The R^2 calculated by the *score* function is given as

$$R^2 = 1 - \frac{\sum_{i=1}^{n}(y_i - f_i)^2}{\sum_{i=1}^{n}(y_i - \bar{y})^2}, \tag{3.3}$$

where n is the number of samples, y_i is the target current density, f_i is the predicted current density and $\bar{y}$ is the mean target current density. An R^2 value of 1.0 indicates a perfect fit.

Another measure of predictive accuracy is the mean absolute error (MAE),

$$MAE = \frac{1}{n}\sum_{i=1}^{n}|f_i - y_i|. \tag{3.4}$$

However, it is important to not rely solely on one of these measures, as they have their strengths and weaknesses. Around the OCP, the current densities will be in the order of 10^{-5}. A predictive error of one decade will have much less impact on the MAE here than in the endpoints of the anodic and cathodic branches. Together with visual inspection, the MAE and R^2 give a good indication of the algorithm's quality of fit.

Chapter 4

Results

4.1 SEM and EDS

All samples were investigated in SEM before electrochemical experiments, and EDS spectra of selected particles were collected. Figure 4.1 shows the surface morphology of the 9506 alloy before and after the brazing heat treatment. Both conditions of the alloy has pits on the surface. EDS spectra of the indicated particles are presented in Table 4.1.

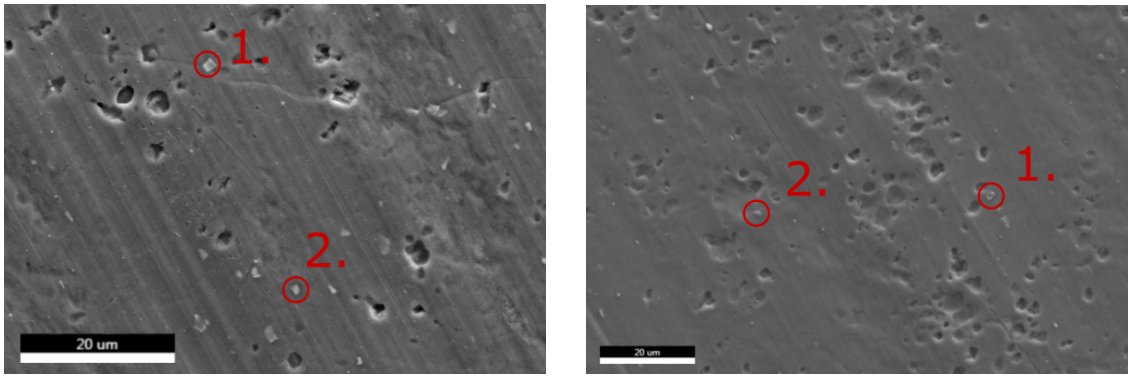

(a) **(b)**

Figure 4.1: SEM images of the surface morphology of **(a)** as-extruded and **(b)** as-brazed conditions of the 9506 alloy before polarisation. Elemental analysis of the two particles indicated in each specimen are presented in Table 4.1.

Particles in both specimens contain Fe, Mn and Si, with some particles also containing small amounts of Cr. The atomic ratio of Fe, Mn and Si suggest that these particles are a mix of Al_6(Fe, Mn) and α-Al(Fe, Mn)Si particles which are common in 3xxx series alloys. The excess Al detected can be attributed to the emission volume being larger than the particle. On the brazed specimen, F and trace amounts of K are detected. The amount of F detected is unreasonably high, however it cannot be ignored as a false signal when K is also detected. Presence of both of these elements simultaneously may indicate remains of flux from the brazing oven.

Figure 4.2b shows the appearance of blisters on the surface of the 1197 alloy after brazing. There are also needle-like precipitates both perpendicular to and in parallel with the extrusion direction. Analysis of these needles with EDS showed the presence of Fe. The

Table 4.1: Quantified EDS analysis for selected surface particles in the 9506 alloy specimens, as shown in Figure 4.1. The reported error % is relative to the reported wt%.

EDS spot	Element	wt%	at%	Error %
9506ar 1	Al	81	88	3
	Si	4.2	4.4	10
	Mn	8.6	4.6	7
	Fe	6.3	3.3	10
9506ar 2	Al	78	86	3
	Si	4.3	4.5	10
	Cr	0.6	0.3	49
	Mn	9.2	5.0	6.6
	Fe	7.9	4.2	8.3
9506b 1	Al	78	86	3
	Si	4.8	5.0	8.0
	Cr	0.9	0.5	17.5
	Mn	8.6	4.7	4.5
	Fe	7.3	3.9	5.0
9506b 2	O	6.4	10.9	8.5
	F	6.4	9.3	9.0
	Al	66	67	3.5
	Si	4.9	4.8	8.0
	K	0.6	0.4	16.5
	Cr	0.7	0.4	19.0
	Mn	8.6	4.3	4.0
	Fe	6.7	3.3	5.5

other surface particles was also enriched with Fe, and EDS spectra only showed trace amounts of Si and Mn as shown in Table 4.2. In comparison, the particles in the alloy before brazing contained appreciable amounts of Mn, with some also containing 2-3 wt% Si.

Figure 4.3b shows the appearance of blisters on the 9170gc alloy in the as-brazed condition. These blisters appear similar to the ones observed on the 1197 alloy in Figure 4.2b. The 9170b specimen on the other hand has more pits on the surface, comparable to those on the 9506b specimen in Figure 4.1b. Such a difference in surface morphology is somewhat unexpected, as the composition of the 9170 and 9170gc alloys are very similar.

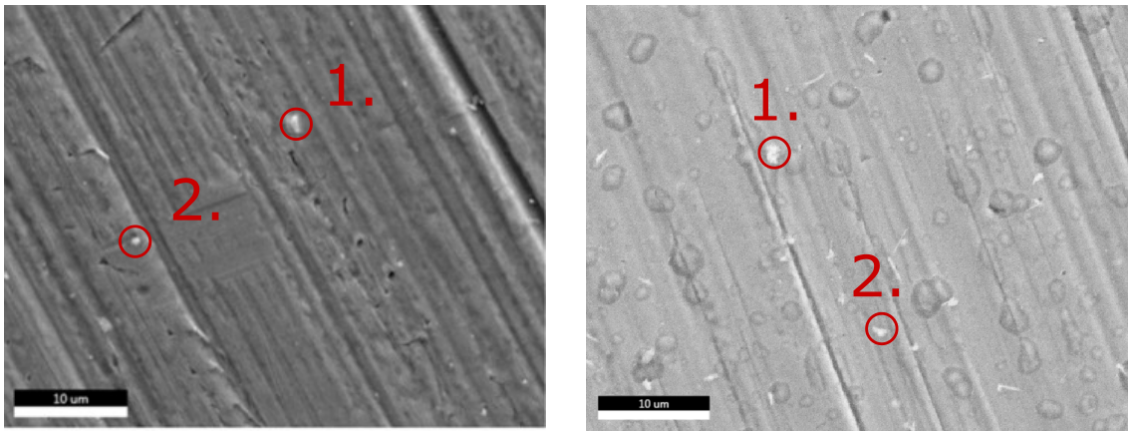

(a) **(b)**

Figure 4.2: SEM images of the surface morphology of **(a)** as-extruded and **(b)** as-brazed conditions of the 1197 alloy before polarisation. Elemental analysis of the two particles indicated in each specimen are presented in Table 4.2

Table 4.2: Quantified EDS analysis for selected surface particles in the 1197 alloy specimens, as shown in Figure 4.2. The reported error % is relative to the reported wt%.

EDS spot	Element	wt%	at%	Error %
1197ar 1	Al	77	87	3.6
	Mn	12.9	7.2	6.0
	Fe	9.8	5.3	7.5
1197ar 2	Al	79	87	3.5
	Si	3.5	3.7	11.0
	Mn	10.8	5.8	5.0
	Fe	7.1	3.8	8.5
1197b 1	O	8.3	15	10
	Al	65	70	4
	Si	0.4	0.5	34
	Mn	2.0	1.1	21
	Fe	24.5	12.9	4
1197b 2	O	6.5	11.4	10
	Al	79	81	3
	Fe	14.7	7.3	5

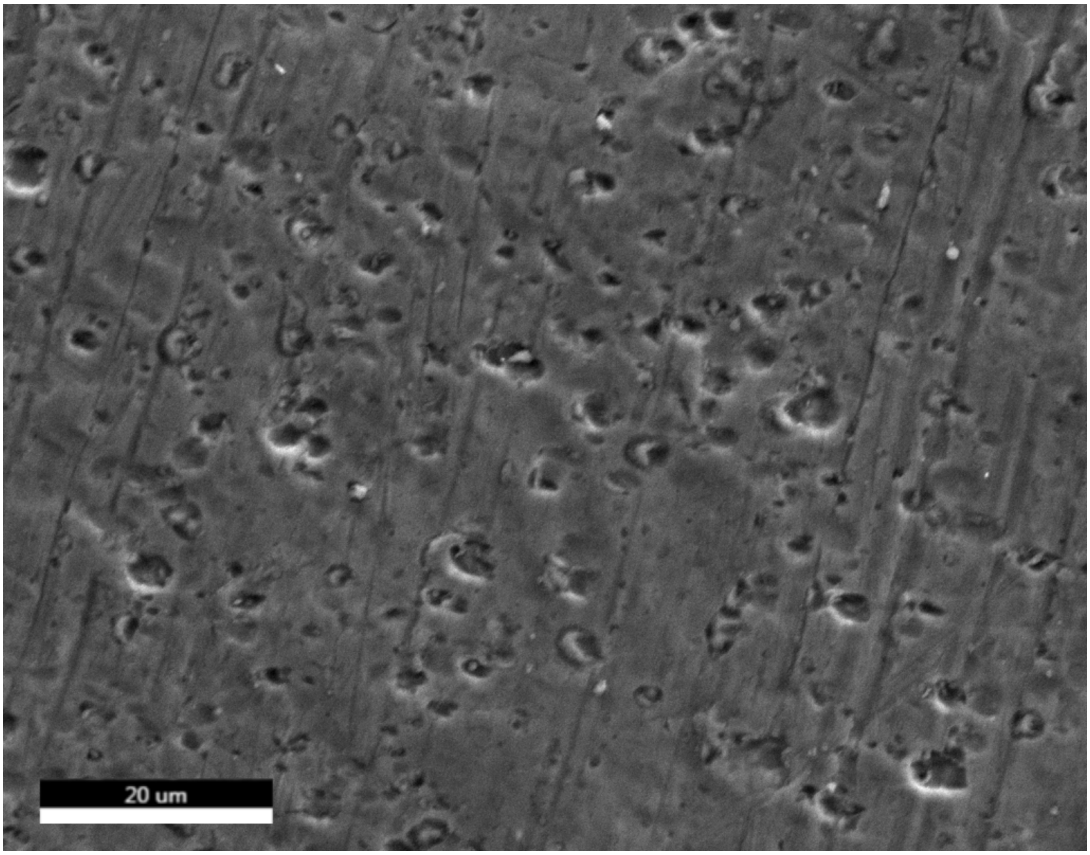

(a)

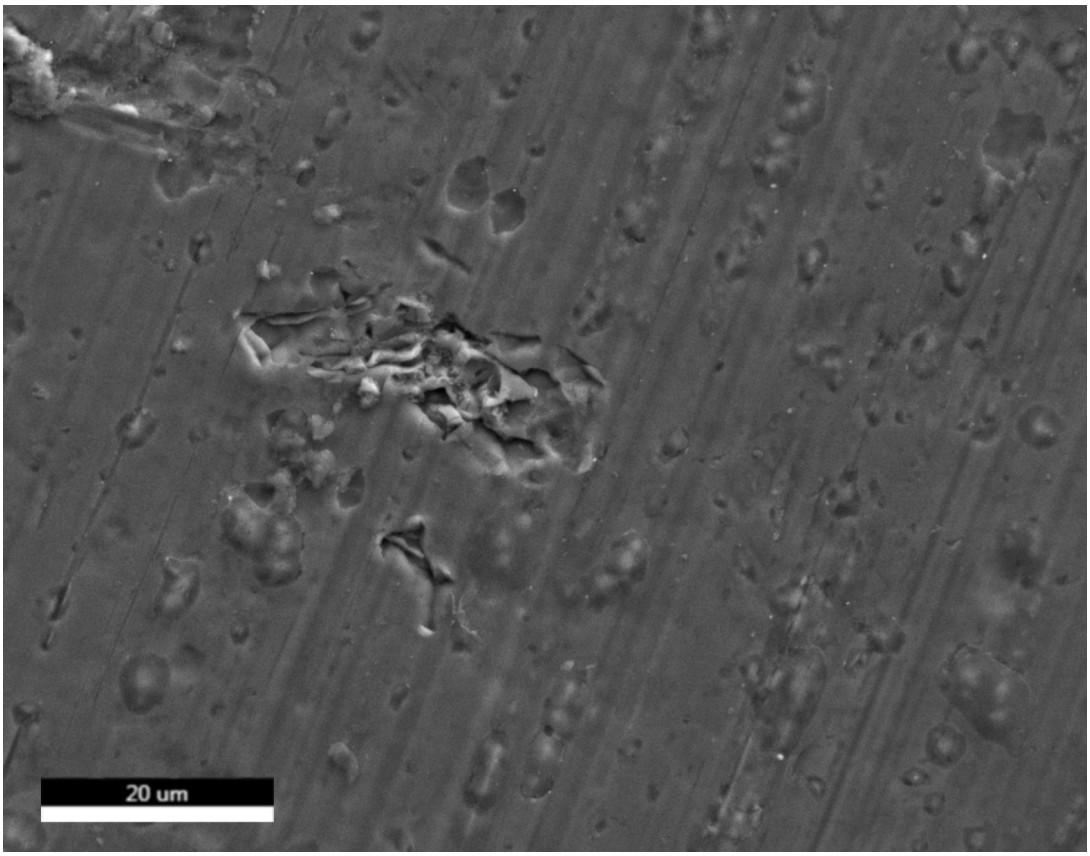

(b)

Figure 4.3: SEM images of the surface morphology of as-brazed condition of the **(a)** 9170 and **(b)** 9170gc alloys before polarisation.

4.2 GD-OES analysis

Surface analysis with GD-OES revealed an enrichment of Pb and Mg in the surface layer of the brazed samples. This is especially present in the 9506 alloy, as shown in Figure 4.4. The surface concentration of Mg reached a concentration as high as 2.5 wt% in the brazed 9506 alloy, which also had the highest bulk concentration of Mg. Of all the alloys, the surface concentration of Pb is also the highest in this alloy.

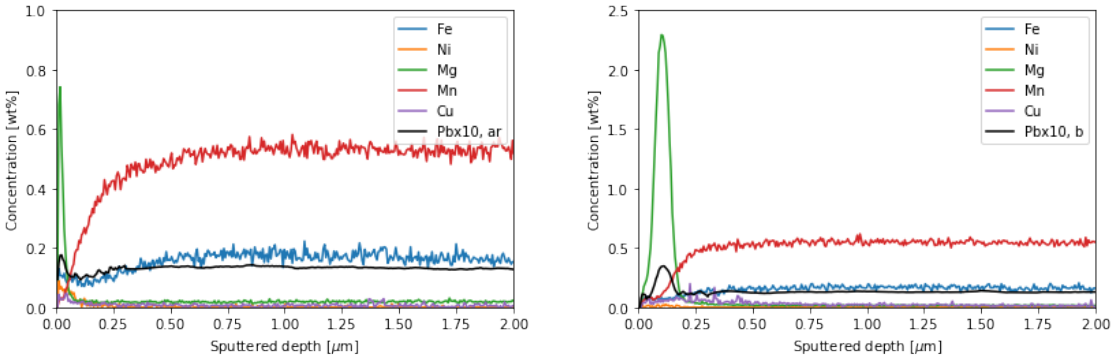

(a) **(b)**

Figure 4.4: GD-OES elemental depth profiles for the **(a)** As extruded and **(b)** As brazed samples of the 9506 alloy.

The 1197 alloy behaved differently from the other alloys. In the as-brazed condition, enrichment of Fe near the surface was found in the 1197 alloy, as shown in Figure 4.5. The measured concentration of Fe reached as high as 0.4 wt% in this sample. There is also a small enrichment of Ni at the surface. Cu on the other hand appears to be depleted near the surface.

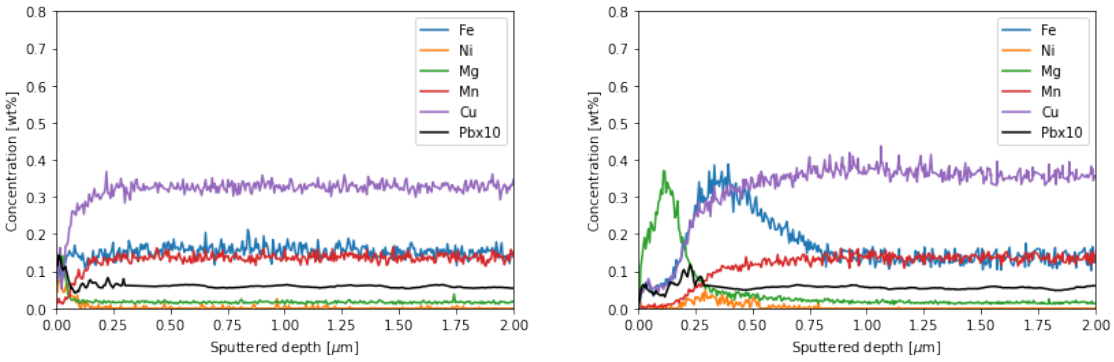

(a) **(b)**

Figure 4.5: Depth profiles for the **a)** As extruded and **b)** brazed samples of the 1197 alloy.

Contrary to the other alloys, enrichment of Pb is not significant in the 1197 specimen. Figure 4.6a shows that there is little difference in surface concentration of Pb between the brazed and as-extruded samples of the 1197 alloy. The enrichment as a result of brazing is most noticeable for the 9506 alloy, but there is also clear enrichment for the 9170 and 9170gc alloys. Generally, the surface concentration of Pb tends to increase with surface concentration of Mg, however there are also some exceptions.

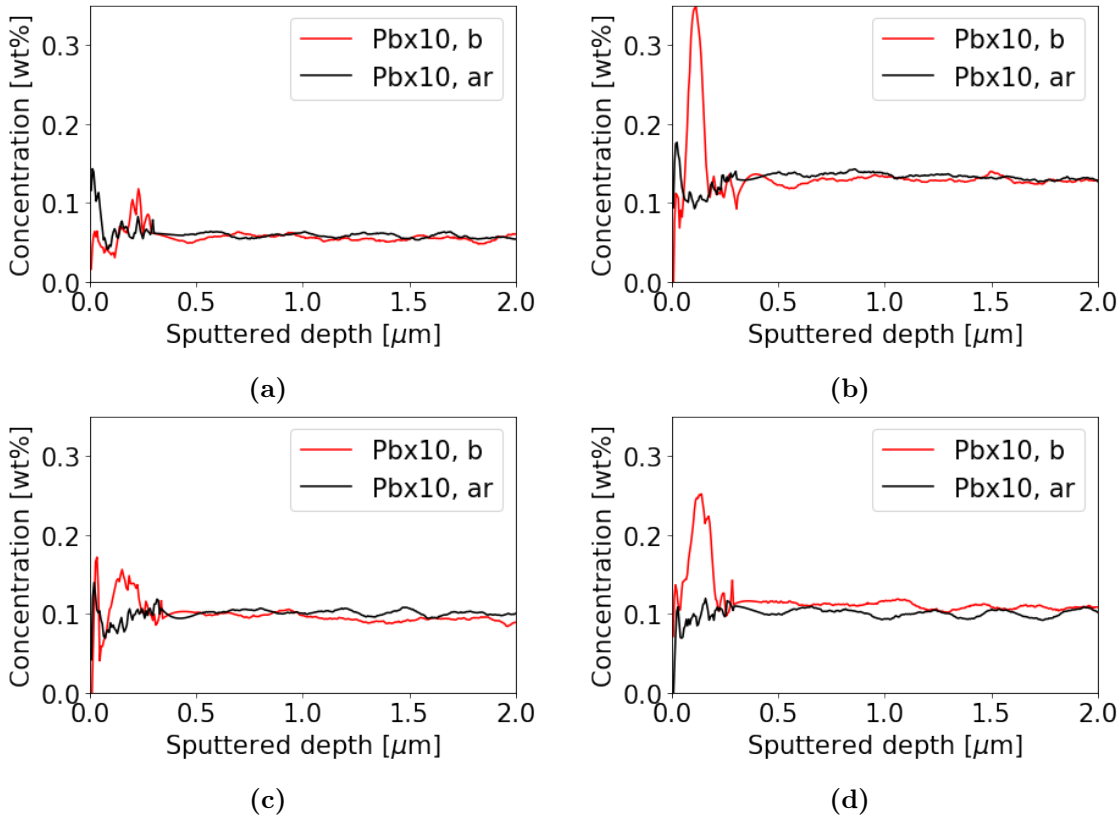

Figure 4.6: Comparison of Pb profiles for as-extruded and as-brazed specimens of the **(a)**1197, **(b)**9506, **(c)**9170 and **(d)**9170gc alloys.

Chemical depth profiles were also recorded for Sn. As shown in Figure 4.7, the brazing heat treatment did not cause segregation of Sn. If anything, the heat treatment caused the concentration of Sn to decrease for the 1197 and 9170gc alloys. Decreased segregation by heat treatment is not expected, as it has been shown that heat treatment at both 300 °C and 600 °C causes segregation of Sn [4].

Chemical depth profiles of the other alloys in this work are presented in Appendix B.

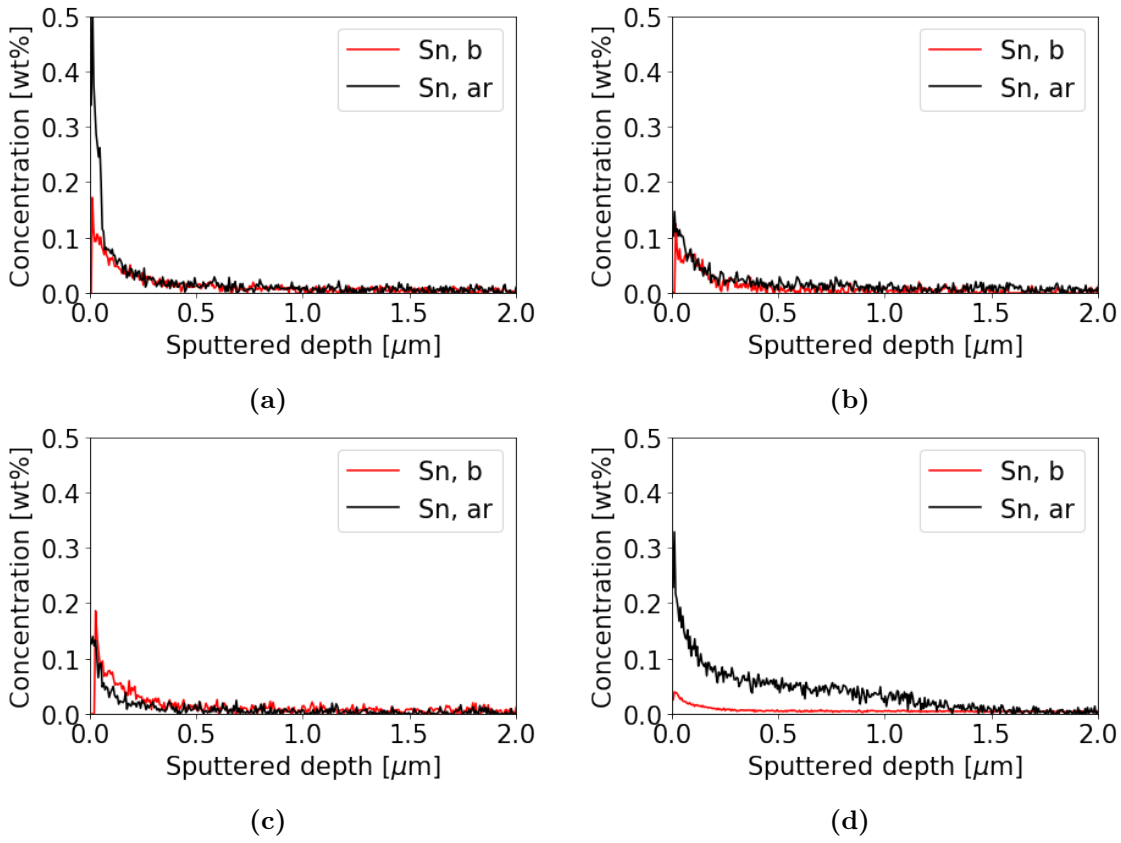

Figure 4.7: Comparison of Sn profiles for as-extruded and as-brazed specimens of the **(a)**1197, **(b)**9506, **(c)**9170 and **(d)**9170gc alloys.

4.3 Potentiodynamic data

The first round polarisation scans for selected alloys in the as-brazed condition are shown in Figure 4.8. Notably, the 1197 alloy shows considerably higher E_{corr} than the other alloys, which all have a similar E_{corr}.

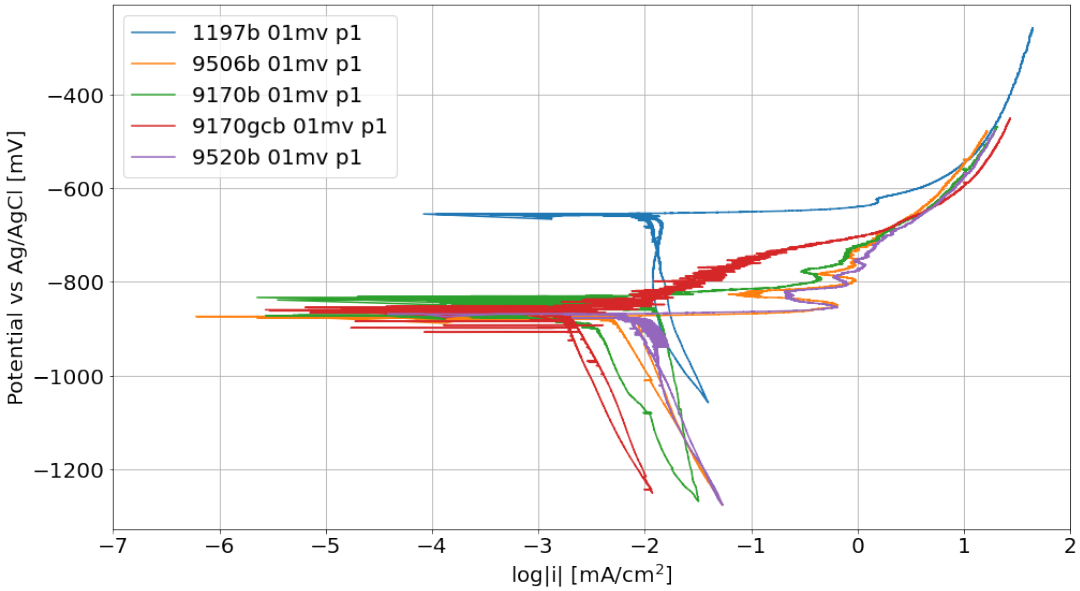

Figure 4.8: Polarisation curves at a sweep rate of 0.1 mV/s in SWAAT solution for selected alloys in the as-brazed condition.

There are also some differences in the shape of the anodic branch of the polarisation curves. The alloys 9506 and 9520 exhibit a pronounced wavy pattern with multiple oxidation peaks. These peaks are not present for the 1197 and 9170gc alloys. The 9170 alloy has less pronounced peaks, and at a higher potential than the 9506 and 9520 alloys.

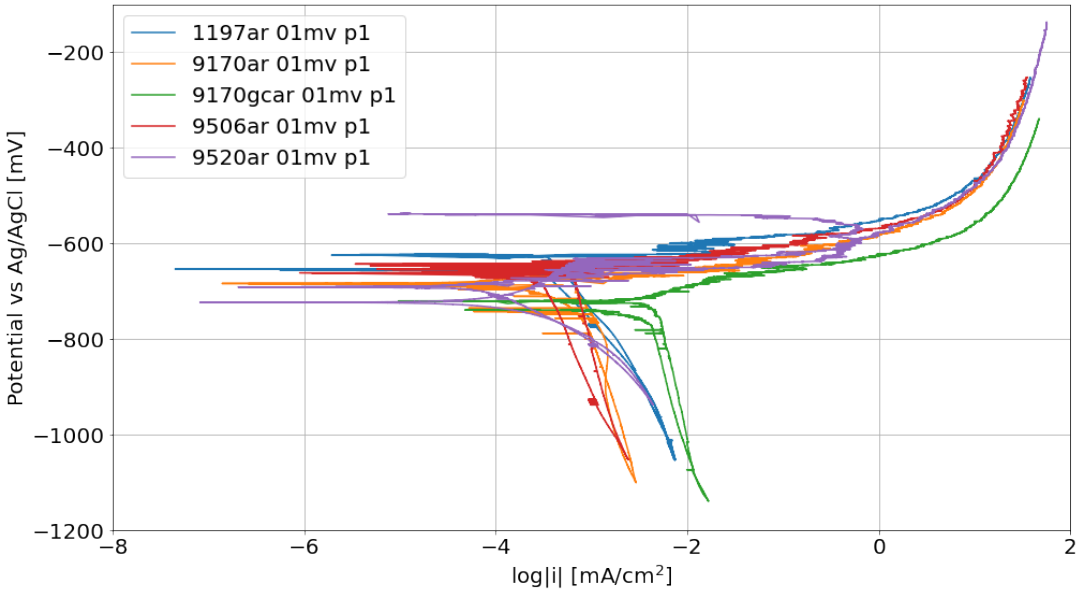

Figure 4.9: Polarisation curves at a sweep rate of 0.1 mV/s in SWAAT solution for selected alloys in the as-extruded condition.

The polarisation curves for the as-extruded specimens contain some noise, as shown in Figure 4.9. This can be attributed to a more unstable E_{corr}. Generally, the as-extruded specimens have a higher E_{corr} than their as-brazed counterparts.

A comparison of the polarisation curves for the as-brazed and as-received conditions of the 9506 alloy is shown in Figure 4.10. In the first round of polarisation, E_{corr} of the as-brazed specimen is 200 mV lower than the as-extruded specimen. After one round of polarisation, there is little difference between the two conditions. E_{corr} is reduced by 50 mV for the as-received sample, while there is an increase of about 150 mV for the as-brazed sample. There is also a significant increase in cathodic current for both samples after the first polarisation scan.

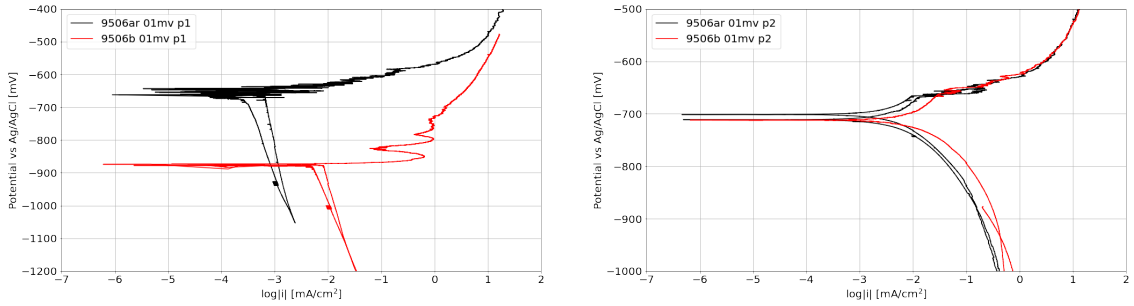

(a) **(b)**

Figure 4.10: Polarisation curves for the **(a)** first and **(b)** second round of polarisation of the 9506 alloy specimens.

In addition to having a more noble E_{corr} than the other brazed alloys, there is also less difference between the as-received and as-brazed samples of the 1197 alloy. As shown in Figure 4.11, the two conditions are not identical in the first round of polarisation, but the shift in anodic current density and pitting potential is less significant compared to Figure 4.10. A more significant difference is observed in the cathodic current density, where the brazed specimen shows an increase of about 1 decade compared to the as-brazed condition.

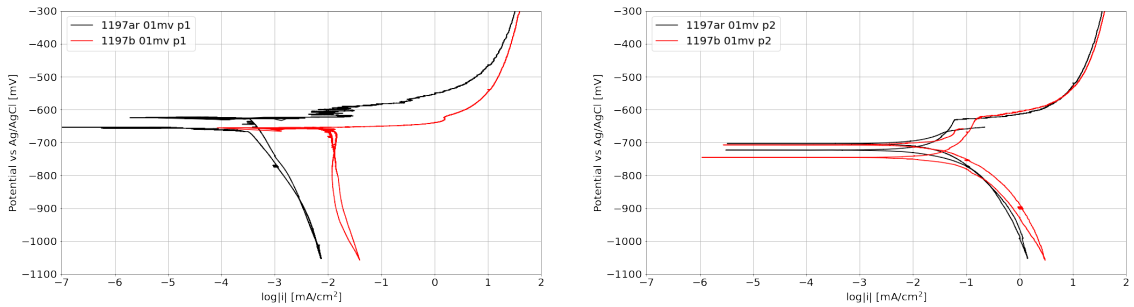

(a) **(b)**

Figure 4.11: Polarisation curves for the **(a)** first and **(b)** second round of polarisation of the 1197 alloy specimens.

A summary of key electrochemical features measured for the alloys in this work is presented in Table 4.3. The table follows the nomenclature given in Figure 3.2, with p1 and p2 referring to the first and second round of cyclic polarisation, respectively.

Table 4.3: Summary of key features in the measured polarisation curves for the alloys in this work. E_{pit} is only reported when there was a clear separation between E_{corr} and E_{pit}. For polarisation curves with two corrosion potentials, the average value is reported.

Alloy	Heat treatment	E_{corr} [mV]		E_{pit} [mV]		i_c [mA/cm^2]	
		p1	p2	p1	p2	p1	p2
1197	ar	-650	-710	-	-630	0.007	1.410
	b	-660	-730	-	-620	0.040	3.033
9170	ar	-680	-760	-	-670	0.003	0.363
	b	-830	-800	-	-660	0.032	1.257
9170gc	ar	-720	-730	-	-680	0.017	0.903
	b	-860	-800	-	-660	0.012	1.044
9506	ar	-660	-710	-	-670	0.002	0.536
	b	-870	-710	-	-660	0.054	2.420
9507	ar	-670	-730	-	-670	0.002	0.397
	b	-860	-820	-	-660	0.022	0.841
9509	ar	-680	-750	-	-670	0.005	0.450
	b	-860	-750	-	-675	0.026	0.860
9520	ar	-720	-750	-630	-670	0.004	0.369
	b	-870	-920	-	-680	0.054	0.336

4.4 ICP-MS

The measured concentrations of selected ions in the electrolyte at different stages of polarisation are presented in Table 4.4. The suffixes an and ocp denote the point at which the samples were taken; ocp refers to samples taken at the corrosion potential after cathodic polarisation, while an refers to samples taken during anodic polarisation (E_{corr}+200 mV). In all samples, the concentration of Cr was below the detection limit of the instrument, and thus Cr is not included in the table.

Table 4.4: Measured concentrations in µg/L of selected alloying elements in the electrolyte after cathodic polarisation and halfway through anodic polarisation. Uncertainties are given as double standard deviations.

Sample	Al	Si	Mn	Fe	Cu	Pb
Blank	480 ± 18	3700 ± 300	15 ± 2	65 ± 5.0	22 ± 4.5	0.52 ± 0.9
1197ar ocp	283 ± 9	4000 ± 500	10 ± 1.7	56 ± 3.0	30 ± 4.0	0.55 ± 0.32
1197ar an	3790 ± 150	4500 ± 400	14 ± 1.6	54 ± 3.0	29 ± 2.0	0.70 ± 1.6
1197b ocp	197 ± 7	4300 ± 350	6 ± 0.7	49 ± 5.0	25 ± 3.0	0.51 ± 1.0
1197b an	4320 ± 109	3800 ± 250	12 ± 2	62 ± 8.0	37 ± 4.0	7.02 ± 1.7
9506ar ocp	94 ± 5	3500 ± 350	5 ± 1.0	43 ± 7.0	5 ± 2.0	1.15 ± 1.2
9506ar an	190 ± 9	3900 ± 350	6 ± 1.1	50 ± 5.0	21 ± 1.5	0.81 ± 1.1
9506b ocp	134 ± 5	3900 ± 300	6 ± 0.9	49 ± 5.0	17 ± 3.5	0.6 ± 0.9
9506b an	652 ± 19	3700 ± 350	7.5 ± 0.6	48 ± 5.0	27 ± 2.0	0.78 ± 0.5

The concentration of Si is relatively high in all samples. This is likely because of contamination from the glassware the samples were stored in. Concentration of all ions are

high in blank sample, which makes it difficult to use the blank sample as a reference. All anodic samples will therefore also be discussed with respect to their respective OCP sample. If assuming little or no cathodic dissolution, there should not be major differences between these samples and the blank sample.

There are no clear trends in the concentration of Fe, and for all samples the concentration is below the concentration of Fe in the blank sample. There is a small increase in concentration of Mn after polarisation in all samples, which correlates well with the expected data in Table 4.5. The only exception is the as-extruded 9506 sample, where expected concentration is much higher than the measured.

Table 4.5: Calculated expected concentrations of the alloy constituents in the electrolyte at the time when the anodic samples were taken. All concentrations are given in µg/L.

Sample	**Q**	**Al**	**Si**	**Fe**	**Mn**	**Cu**	**Pb**
1197ar	7.8 C	723	1.7	4.1	3.3	11.2	0.46
1197b	12.2 C	1130	2.7	6.4	5.2	17.5	0.72
9506ar	5.0 C	464	2.0	2.5	8.3	0.03	0.69
9506b	0.8 C	71	0.3	0.4	1.3	0.01	0.11

The concentration of Al was the highest in the two samples taken of the 1197 alloy at -410 mV and -450 mV, respectively. An increased concentration of Al in these samples is expected, as the calculated total charge were the highest in these samples. However, the measured concentration is in both cases considerably higher than what is expected based on the calculated charge.

Increased concentration of Pb after anodic polarisation was only noticeable in the 1197b specimen. For this sample, concentration increased by 6.5 µg/L relative to both the blank sample and the ocp sample. Compared to the expected concentration, the measured Pb concentration is almost 10 times higher.

4.5 Corrosion morphology

After three rounds of polarisation, both the as extruded and as brazed specimens of the 9506 alloy show signs of crystallographic pitting corrosion. The corrosion morphology of these samples are shown in Figure 4.12.

In the case of the as extruded specimen, deep pits have gone all the way through the specimen. For the as brazed sample, the pits were not as deep. Some corrosion also appears to have occurred along the grain boundaries, as indicated by the arrows in Figure 4.12b.

Many of the brazed samples had surfaces with visible spangle after polarisation, not unlike that of galvanised steel. This is likely a result of etching by the acetic acid. The as-received samples had deep holes, some of which had propagated all the way through the sample. The localised nature of the corrosion attack on the as-extruded 9506 alloy compared to the brazed condition is shown in the low-magnification SEM image in Figure 4.13.

Samples of the 9170 and 9170gc alloys in the as-brazed condition were examined in SEM after one round of polarisation. Both samples show signs of crystallographic pitting, as

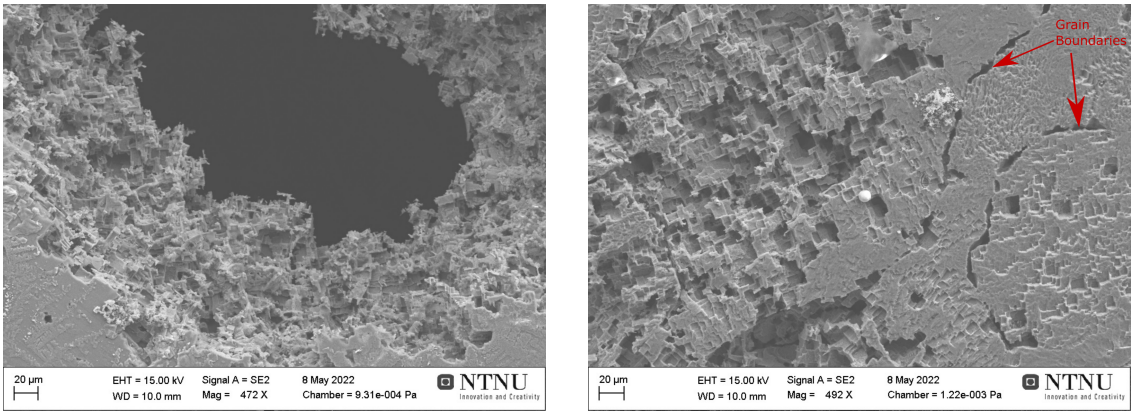

(a) **(b)**

Figure 4.12: Corrosion morphology for the **(a)** 9506ar and **(b)** 9506b specimens after three rounds of cyclic polarisation in acidified synthetic seawater.

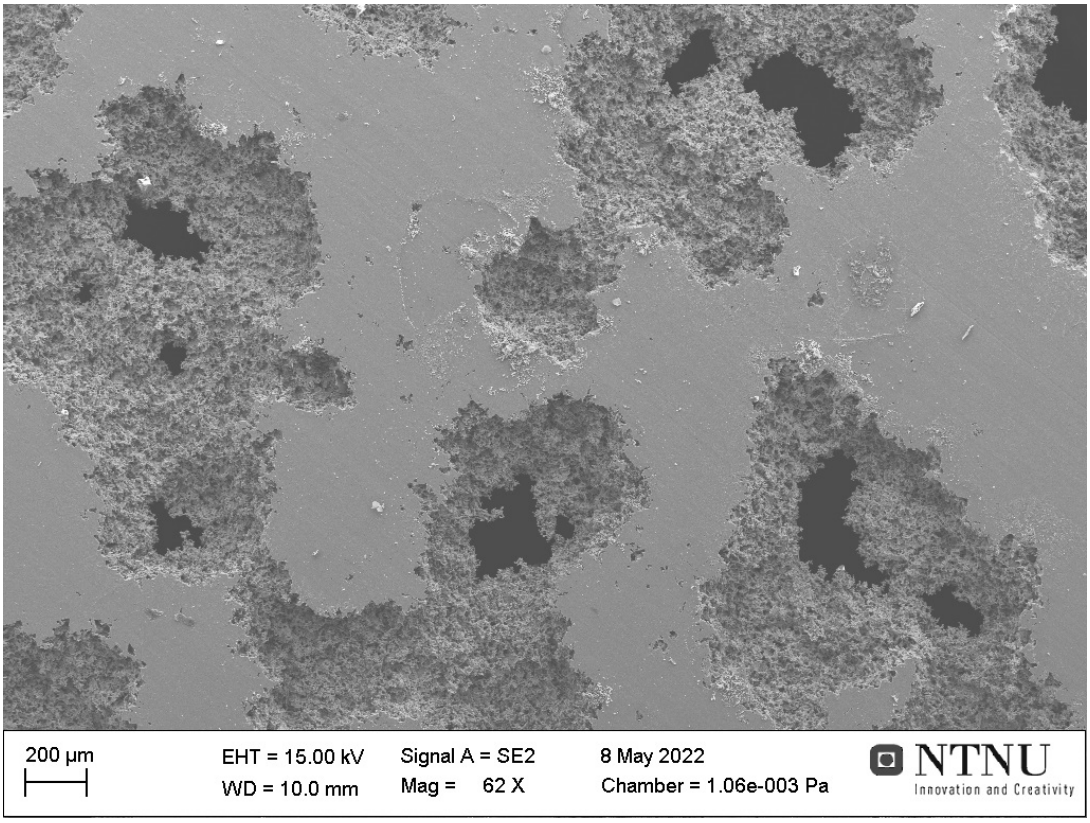

Figure 4.13: SEM image of the corroded surface of the 9506ar specimen after three rounds of polarisation at a sweep rate of 0.1 mV/s in acidified synthetic sea water.

shown in Figure 4.14. Some selective dissolution around cathodic particles also appear to have occurred on both samples.

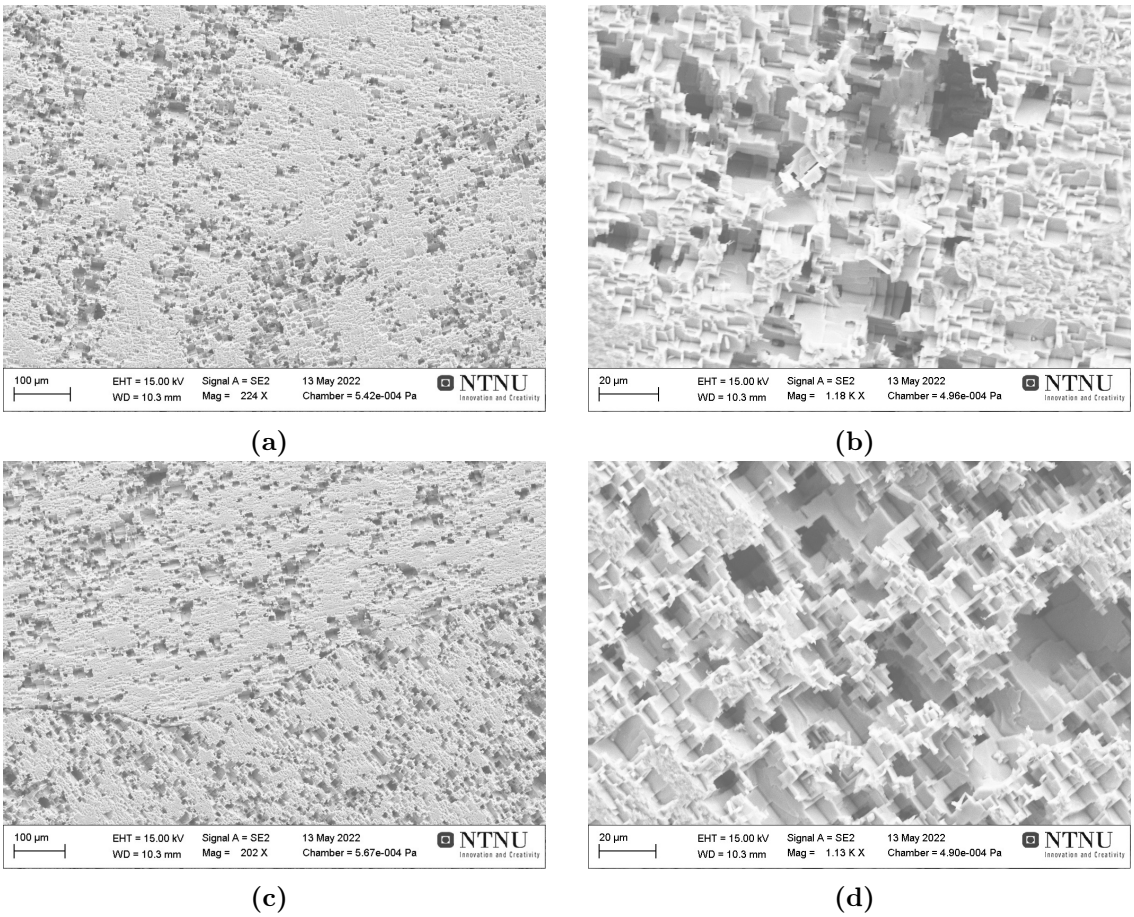

Figure 4.14: Corrosion morphology for the **(a)**, **(b)**9170b and **(c)**, **(d)**9170gcb specimens after one round of anodic polarisation at a sweep rate of 0.1 mV/s in acidified synthetic sea water.

4.6 Machine learning

Predicted polarisation curves for the 9506b specimen after one and three rounds of polarisation are shown in Figure 4.15. For this prediction, all data sets in Table 3.4 except 9506b r1 were used. The algorithm is able to predict the polarisation curve accurately for the third round of polarisation. Crucially, the predicted curve for the initial round of polarisation is not as accurate. Especially the predicted values around E_{corr} are somewhat off, probably influenced by the 9108 and 9510 alloys where a more noble corrosion potential was measured.

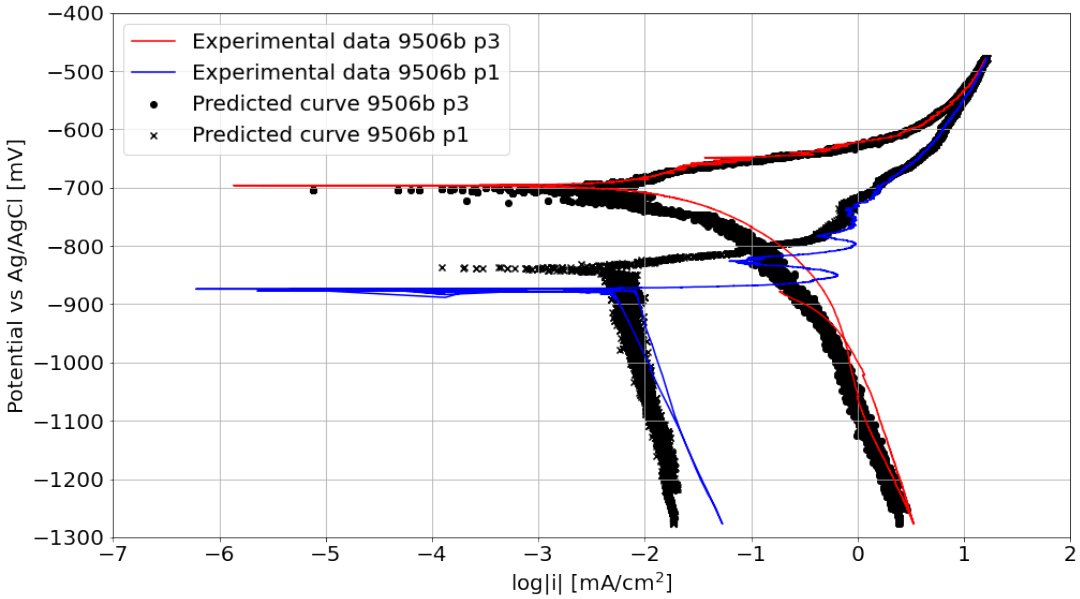

Figure 4.15: Predicted polarisation curves after one and three rounds of polarisation at a sweep rate of 0.1 mV/s in SWAAT solution for the as-brazed 9506 specimen. The suffixes p1 and p3 refers to the first and third round of polarisation, respectively.

The weighting of each input feature when omitting the 9506b data set is shown in Table 4.6. With less than 0.03% weight each, Mg, Ti and Cr are insignificant when predicting the polarisation curves.

Table 4.6: Feature importance for the model when data for the 9506b specimen was left out of the training set.

Feature	**Weighting [%]**
Si	0.73
Fe	0.66
Mn	0.15
Mg	0.03
Ti	0.02
Cr	0.02
First?	1.48

Calculated values for R^2 and MAE for the predicted 9506b curves are shown in Table 4.7.

The higher MAE value observed for the p3 curve compared to the p1 curve can be attributed to the increased cathodic current density for the p3 curve.

Table 4.7: Measures of quality of fit for the predicted curves for the 9506b specimen.

Curve	R^2	MAE
9506b p1	0.804	0.131
9506b p3	0.984	0.298

The modified model with Cu content as input feature was used to predict the polarisation curves for the 1197b specimen. As Figure 4.16 shows, the predictive accuracy on this alloy is poor. This is however expected, as the corrosion potential for this alloy is much nobler than the rest of the alloys in the dataset. The 1197 alloy is also the only alloy with an appreciable amount of Cu, so when this dataset is omitted the model is only trained on alloys with low Cu content.

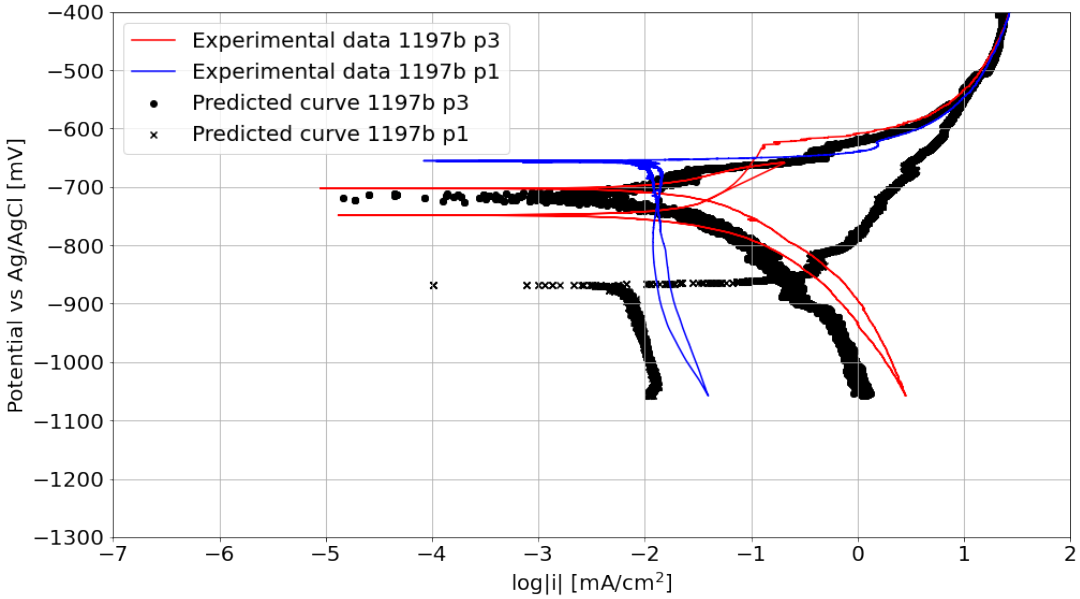

Figure 4.16: Predicted polarisation curves after one and three rounds of polarisation at a sweep rate of 0.1 mV/s in SWAAT solution for the as-brazed 1197 specimen. The suffixes p1 and p3 refers to the first and third round of polarisation, respectively.

Calculated values for R^2 and MAE for the predicted 1197b curves are shown in Table 4.8. Compared to the visual assessment of the quality of fit, the calculated R^2 is unreasonably high, especially for the p1 curve.

Table 4.8: Measures of quality of fit for the predicted curves for the 1197b specimen.

Curve	R^2	MAE
1197b p1	0.951	1.156
1197b p3	0.948	2.162

Polarisation curves for the as-extruded specimens were also predicted using the modified model. Figure 4.17 shows the predicted curve for the 9506ar specimen. The polarisation

curve for the 9509ar specimen, which was part of the training set for this specific iteration, is also shown. It is clear from the figure that for the anodic and cathodic ends of the curve, the predicted curve is similar to the one of the 9509 alloy. This can be attributed to the similarity in alloy composition between the 9506 and 9509 alloys.

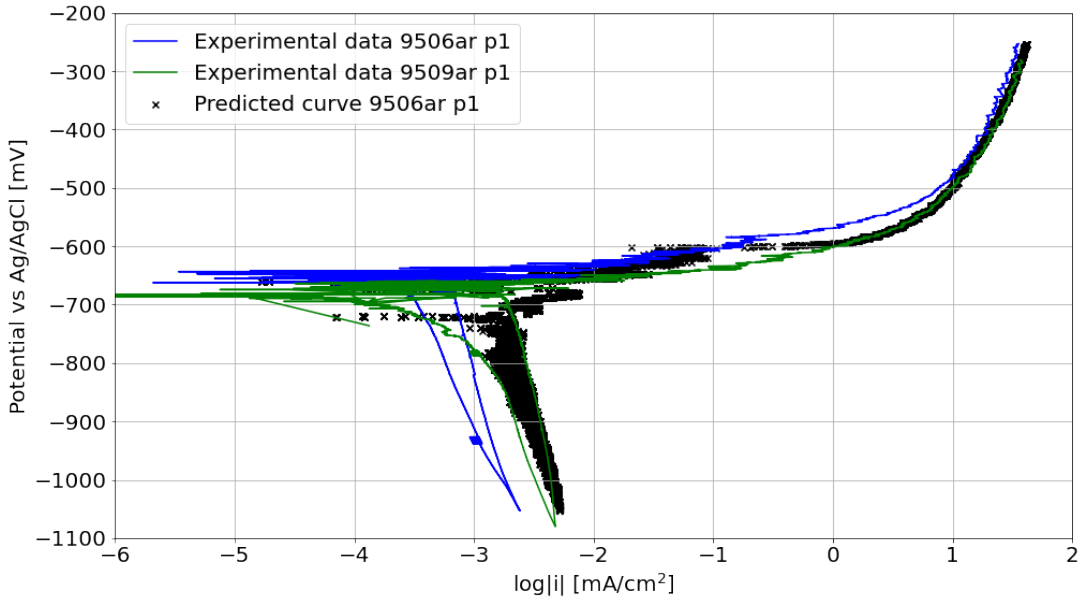

Figure 4.17: Predicted polarisation curve after one round of polarisation at a sweep rate of 0.1 mV/s in SWAAT solution for the as-extruded 9506 specimen.

However, the predicted curve for the third round of polarisation shown in Figure 4.18 is not as influenced by the 9509ar data. Both the area around the corrosion potential and the anodic and cathodic branches are described well.

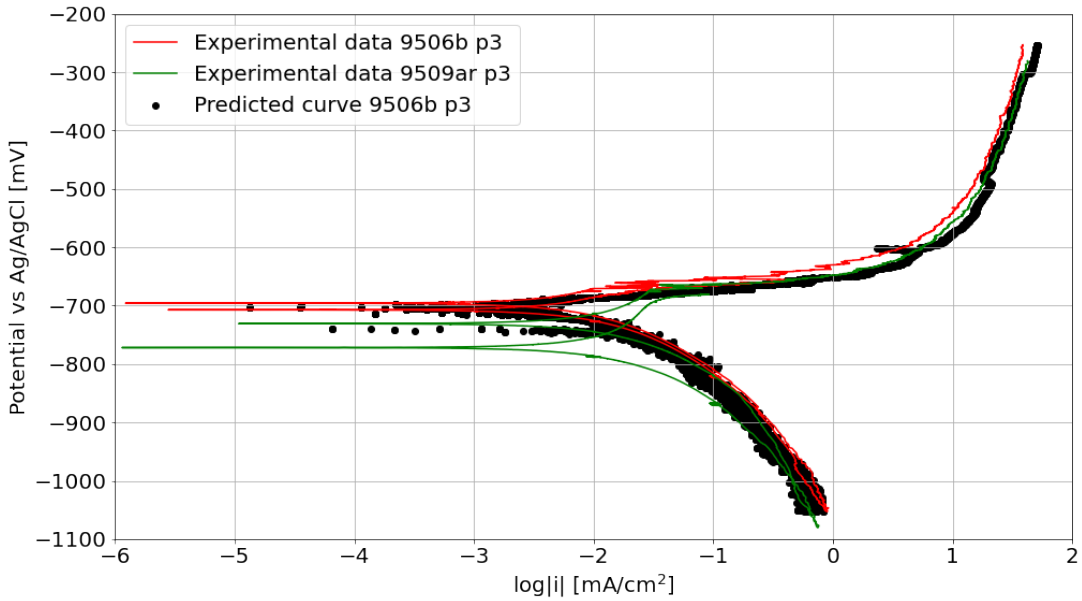

Figure 4.18: Predicted polarisation curve after three rounds of polarisation at a sweep rate of 0.1 mV/s in SWAAT solution for the as-extruded 9506 specimen.

Interestingly, the weighting of the input parameters are different for the model for the

as-extruded samples, as shown in Table 4.9. There is an increased emphasis on Si and the "First?" binary variable, while the weighting of the potential and Fe parameter are decreased.

Table 4.9: Feature importance for the model when data for the 9506ar specimen was left out of the training set.

Feature	**Weighting [%]**
Si	1.49
Fe	0.06
Mn	0.32
Cu	0.11
First?	2.24

Chapter 5

Discussion

5.1 Segregation of Pb and Sn

The temperature in the brazing treatment is high enough to cause segregation of Pb, therefore enrichment is expected. The amount of segregation will be limited by the short holding time at 600°C. However, the alloys also contain some Mg which will increase segregation at lower temperatures. The combination of time and temperature in the brazing cycle is enough to cause significant segregation of Pb at the surface, leading to significant anodic activation of the aluminium alloys. No Pb or Sn were detected in the surface particles analysed with EDS.

An unexpected effect of the brazing heat treatment is reduced segregation of Sn for some alloys. However, the measured concentration of Sn in the selected samples is unreasonably high. Reaching concentrations close to 0.4 wt% for the 1197 and 9170gc samples, the concentration of Sn is comparable to the concentration of the main alloying elements. The concentration of Sn in commercial recycled alloys usually only reaches about 100 ppm [4]. A possible explanation for the high concentrations is contamination by Sn in the lab, which was also observed in other works in the same laboratory. Another source of error could be the conversion to wt %. If the actual concentration of Sn in the calibration sample was lower than stated, the conversion to wt% would result in a higher concentration than what is actually the case. However, errors in calibration does not change the fact that surface concentration of Sn was higher in the as-received condition of the 1197 and 9170gc alloys. Anodic activation in these alloys can therefore not be explained by segregation of Sn.

5.2 Effect of Cu on anodic activation

There is little difference in electrochemical behaviour observed between the as-extruded and as-brazed samples of the 1197 alloy. This is in line with previous work on this topic, which showed that the addition of Cu in the alloy is effective for mitigating the effects of the group IIIA-VA trace elements [5]. However, the GD-OES results suggest that Cu was depleted near the specimen surface. Some Cu enrichment is still expected during polarisation, as selective dissolution of Al will result in an ennobled surface. According to Anawati et al. [6], the cause of the reduced activation could be predominantly due

to ennoblement of the alloy surface by the added Cu. However, the GD-OES results in this work indicate that the addition of Cu also affected the degree of surface segregation of elements like Pb. This is further supported by the fact that the polarisation curves for the as-extruded and as-brazed 1197 specimens were so similar. The largest difference in the measured corrosion potential in the present study was less than 30 mV, while in the study by Anawati et al. [6] the difference between an AlPbCu alloy and an AlCu alloy containing 0.2 wt% Cu was in the order of 100 mV. Furthermore, the alloys not containing appreciable amounts of Cu are equally ennobled by other alloy elements in the as-extruded condition.

ICP-MS results indicate that dissolution of Pb is the highest in the 1197b specimen. The measured concentration of Pb is 10 times higher than what is expected based on total charge. This indicates that either selective dissolution of Pb occurred, or that the surface concentration of Pb in this sample was higher than what was measured by GD-OES. Thermodynamically, dissolution of Pb is not expected. Compared to observed E_{corr} of Al in this work, the oxidation reaction of Pb to Pb^{2+} has a much higher reversible potential of -0.33 $V_{Ag/AgCl(\text{sat. KCl})}$ [33].

Dissolution of Cu appears to occur independent of bulk composition based on the ICP-MS results. Part of this may be due to a small depletion of Cu near the surface in the 1197 samples. Selective dissolution of Cu is not expected since it is the most noble of the alloying and trace elements present. However, it has been observed in other works in this laboratory that Cu also dissolves in significant amounts in AA6060 alloys [62].

The highest dissolution of Al occurs in the 1197ar and 1197b samples, with measured concentrations of Al being close to 4 mg/L. Increased concentration of Al in these samples is expected because of higher total current, however the measured concentration is about 3 mg/L larger than what is expected by integration of the polarisation curve. This can not be explained solely by the assumption of uniform dissolution. Electrolyte samples were collected in the middle of the electrochemical cell. As corrosion occurs, there is likely to be a concentration gradient in the solution. Near the electrode surface the concentration of corrosion products will be higher than in the bulk solution, especially when there is no stirring in the cell. As such, the sampled electrolyte might not represent the bulk electrolyte. A way of getting more representative and insightful results by use of ICP-MS would be to study the electrolyte concentration in-situ while running the electrochemical experiments. In this way one can avoid problems with contamination, while also monitoring the establishment of a concentration gradient.

A weakness of this study is the fact that all alloys studied are commercial alloys. The possibility of local variations in alloy composition therefore exists. GD-OES results might therefore have a certain deviation from the actual concentration in the region where electrochemical experiments were conducted, and thus not be representative for the measured polarisation curves. Bulk concentration of trace elements might also vary from alloy to alloy. This is difficult to control, as reproducing polarisation data for aluminium alloys in chloride containing solutions is known to be difficult. Both the cyclic polarisation scans and GD-OES measurements are also destructive to the samples, so doing both on the same sample would not be possible.

5.3 Corrosion morphology

As observed by Gundersen et al. [28], lead enrichment on the surface mitigated pitting corrosion to some degree. By visual inspection of the samples after polarisation, there are clear signs of pitting on the as-received samples. Samples in the brazed condition however showed a spangled, almost grain-like surface. More thorough investigation of the corrosion morphology in SEM revealed typical signs of crystallographic pitting on both sample conditions. The lack of pitting observed visually is therefore likely to be due to other types of corrosion occurring on the brazed samples, masking the pitting. When activated, a larger surface area will be attacked. Since the current is distributed over a larger area, the corrosion will appear more uniform. The as-extruded specimens don't experience the same broad attack, and the local attacks are thus more severe.

It can be argued that the added resistance against pitting corrosion can outweigh the effect of increased activation in service. In heat exchanger applications, avoiding leakage of the coolant fluid is paramount, thus pitting is undesirable. However, one also needs to take into account that the increased activity could lead to galvanic corrosion between the different aluminium parts of the heat exchanger. The construction should therefore be designed accordingly. Controlling the concentration of trace elements in commercial production of aluminium could, however, be difficult.

5.4 Absence of oxidation peaks

The polarisation curve for the 1197 alloy does not exhibit a wavy pattern in the anodic branch, contrary to what was found by Sævik [5] and Anawati et al. [6]. The levelling of the oxidation peaks in the anodic branch of the polarisation curve may be attributed to the presence of other alloying elements like Fe and Si. Especially Fe is of interest, as it became enriched on the surface of the sample in the brazed condition. This enrichment did not occur in any of the other samples. EDS spectra showed both needle-like precipitates containing Fe and also Fe-rich particles on the surface of the 1197b sample. These particles are likely the source of the enriched Fe. Previous work has attributed the reduced activation to Fe in solid solution. However, the Fe needles could possibly also act as sites for underpotential deposition of Pb at the surface, similar to what was suggested for Cu by Sævik [5, 63]. In addition to the ennobling effect of Cu, it is likely that the Fe needles also contribute to ennoblement of the surface. However, it might also be the case that the scan rate of 0.1 mV/s is too fast to detect the oxidation peaks for the 1197b sample. A scan rate of 0.1 mV/s is in principle a slow scan rate, but it has been shown in other work that this is sometimes too fast to obtain a clear resolution of the peaks [43].

The polarisation curves for the 9170b and 9170gcb samples are considerably different, even though their chemical composition are more or less identical. In particular, the absence of oxidation peaks for the 9170gcb specimen is of interest. GD-OES analysis showed that there are small differences in the surface compositions as well. 9170b had more Mg and less Pb, which is somewhat unexpected as Mg enhances segregation of Pb [7]. The oxidation peaks observed for 9170b are also closely connected to the presence of Pb, so the absence of such peaks in the polarisation curve for 9170gcb is unexpected. Post-mortem SEM analysis after one round of polarisation showed no observable difference in corrosion morphology of the two samples.

The absence of oxidation peaks in the polarisation curves for the 1197b and 9170gcb specimens might be related to the blisters observed on the surface of these samples. However, when analysed with EDS, only aluminium and oxygen was detected in the blisters. The cross-section of the samples were not investigated, so it is unknown whether or not the blisters are hollow. However, blisters have previously been reported to occur in model aluminium alloys containing small amounts of In [29]. It was suggested that these blisters were due to In diffusing back into the Al matrix. It is possible that a similar mechanism is responsible for the behaviour observed by the 9170gcb and 1197b specimens. Diffusion of trace elements away from the surface will reduce anodic activation, and thus also possibly level the characteristic oxidation peaks.

5.5 Other factors influencing the polarisation curves

Some of the EDS spectra detected trace amounts of fluoride and potassium on the brazed samples. This likely stems from the oven where the brazing was done. A flux of potassium fluoroaluminate is commonly used to remove metal oxides at the brazing temperature, without reacting with the metals to be joined. Since the oven is in regular use for actual brazing processes, leftover flux might have been adsorbed to the oven walls. When reheated, this flux might have reacted with the alloy surface. Fluoride ions are known to be corrosive to aluminium [64], however since the electrolyte already contains large amounts of chloride ions it is unlikely that the polarisation curves are affected much by the fluoride. Moreover, there does not seem to be a correlation between the samples where fluoride and potassium were detected and electrochemical behaviour. Investigation of any reaction occurring between the fluoride and aluminium at high temperatures were outside the scope of this master's thesis.

Presence of oxygen in the electrolyte could have influenced the results. Purging with N_2 is not guaranteed to remove all dissolved oxygen from the solution. Oxygen could also dissolve into the electrolyte during the experiments. It has been shown earlier that the contribution from the ORR on the anodic current density is insignificant. However, cathodic current density and E_{corr} would likely be affected by presence of oxygen in the electrolyte.

5.6 Machine learning

The polarisation curves of both the as-extruded and as-brazed alloy conditions were predicted with good accuracy by the machine learning model. For some of the curves, there are signs of overfitting. This is especially true for Figure 4.17, where large parts of the anodic and cathodic branches of the polarisation curve seems to be based on polarisation curve for the 9509ar alloy, which was in the training set when predicting the 9506ar curve. For other curves, the model adapts well to the new data. The machine learning algorithm is not able to predict the initial polarisation curve for the 1197b sample, which contains Cu. This is not surprising, as this curve exhibit considerably different behaviour than the rest of the alloys. For prediction of the 1197 alloy to be accurate, one would probably need to include one (or more) alloys with varying Cu content.

For the 9506 alloy in the brazed condition, the algorithm is able to predict the polarisation curves quite well. In addition to visual assessment, the calculated value for R^2 for the p3

curve of 0.98 indicate high predictive accuracy. Since this alloy has a similar composition to several of the alloys in the training set, increased predictive accuracy is expected. On the other hand, some of the predicted curves for the as-extruded alloys show signs of overfitting.

Because of the logarithmic nature of the polarisation curves, calculated values for R^2 and MAE can in some cases be misleading. This is shown very clearly for the case of the 9506 alloy, where even though the predicted third polarisation curve outperforms the predicted p1 curve visually and by means of R^2, the calculated MAE is higher. The limitations of R^2 become even clearer when considering the calculated values for the predicted 1197 curves. Visually, the predicted p1 curve is not at all close to the actual experimental data, however R^2 is as high as 0.95. Therefore, more emphasis should be put on the visual assessment of the curves rather than the qualitative measures.

An interesting point is that the model put more emphasis on distinguishing between the first and non-first rounds of polarisation for the as-extruded samples than for the as-brazed samples. This is unexpected considering the anodic activation occurring for the as-brazed samples, as discussed in the previous section. However, it might be the case that the difference from first to second polarisation is more uniform for the as-extruded alloys. For instance, among the as-brazed samples, both the 9520 and 1197 alloys exhibited behaviour different from the rest of the alloys.

The computation time for the machine learning algorithm increases with the amount of input data. A way to circumvent this could be to tailor new input features based on some chosen parameters. In the study of corrosion rates, this was done successfully by using different chemical data inherent to each alloy element such as electronegativity and thermal conductivity [57]. For the polarisation curves, possible input features could be E_{corr}, i_{corr} and E_{pit}. Data from GD-OES might also be relevant to include in these features. Especially for predicting the initial polarisation curve, the surface alloy chemistry might be more useful input data than the bulk composition. A simpler approach is to coarsen the sampling of data. The obvious pitfall here is to omit areas of particular importance, as discussed in section 3.6.1.

Due to the specific nature of which the algorithms in scikit-learn have to receive input data, it might be the case that better results can be achieved with tailored algorithms. The input data in scikit-learn is given as a matrix, where each row contains the features and answer. This means that for each polarisation curve, a lot of input rows are needed, and a lot of them will be nearly identical. For the polarisation curve for 9506b, each row will contain the alloying elements, and have small variations in E and i, i.e. there are multiple rows that are more or less identical. This is also the reason that the present algorithms are better suited for applications like corrosion rate, where each row is unique. Creating new algorithms for machine learning were however outside the scope of this masters thesis.

5.7 Further work

The author suggests the following further work:

- The effect of copper on enrichment of group IIIA-VA trace elements and anodic activation in commercial alloys should be investigated in more detail.

- In-situ study of corrosion with ICP-MS should be explored.
- The possible role of blisters in levelling anodic oxidation peaks should be investigated.
- The training data for the machine learning model should be expanded with more Mn-containing Al-alloys.
- Tailored algorithms and input parameters should be explored to achieve better performance.

Chapter 6

Conclusion

Pb, which segregated to the surface as a result of a brazing heat treatment, was found to be the cause of anodic activation in a series of commercial Mn-containing aluminium alloys. Alloyed Cu reduced the effect of anodic activation by Pb in the commercial aluminium alloys. Experiments conducted to reveal the mechanism of the reduced activation were inconclusive. On one hand, chemical depth profiles collected with GD-OES suggested insignificant segregation of Pb in the as-brazed sample. On the other hand, analysis of the electrolyte by ICP-MS indicated a concentration of dissolved Pb 10 times higher than what was expected based on theoretical calculations.

Differences in electrochemical behaviour between the 9170b and 9170gcb specimens, two alloys of very similar composition, could not be explained by alloy composition or GD-OES depth profiling. Post-mortem SEM analysis of the two alloys after one round of polarisation did not show any observable differences between the two samples. The possible role of surface blisters in levelling the oxidation peaks was suggested.

The work laid out suggests the potential of using machine learning for predicting polarisation curves for aluminium alloys, using the alloy composition as input parameter. To achieve success in this pursuit, the alloys included should be carefully selected. Include too many different alloys, and the amount of data points will become a problem for the execution speed of the algorithm.

The work raised new questions in terms of understanding the mechanism behind the reduced anodic activation, regarding whether or not Cu contributes to decreased segregation of Pb. The developed machine-learning algorithm can - with appropriate training data - be used to study the effect of alloy element variations on electrochemical behaviour in structurally relatively similar alloys. Such variation are e.g. highly relevant for alloys based on recycled material, as the corresponding alloys have a potentially larger composition window.

Bibliography

[1] The European Commission, *Communication from the Commission to the European Parliament, the European Council, the Council, the European Economic and Social Committee and the Committee of the Regions - The European Green Deal. COM(2019) 640 final.* The European Commission, 2019.

[2] M. Pourbaix, *Atlas of Electrochemical Equilibria in Aqueous Solutions.* Pergamon Press, 1966.

[3] A. Afseth, J. H. Nordlien, G. M. Scamans, and K. Nisancioglu, "Effect of heat treatment on electrochemical behaviour of aluminium alloy AA3005," *Corrosion Science*, vol. 44, pp. 145–162, Jan. 2002.

[4] J. Tan and K. Nisancioglu, "Effect of small amounts of alloyed tin on the electrochemical behaviour of aluminium in sodium chloride solution," *Corrosion Science*, vol. 76, pp. 219–230, Nov. 2013.

[5] Øystein Sævik, *Dissertation, NTNU 2005:125.* PhD thesis, NTNU, Trondheim, Norway, June 2005.

[6] Anawati, S. Diplas, and K. Nisancioglu, "Effect of Copper on Anodic Activity of Aluminum-Lead Model Alloy in Chloride Solution," *Journal of The Electrochemical Society*, vol. 158, p. C158, Mar. 2011. Publisher: IOP Publishing.

[7] Z. Jia, B. Graver, J. C. Walmsley, Y. Yu, J. K. Solberg, and K. Nisancioglu, "Effect of Magnesium on Segregation of Trace Element Lead and Anodic Activation in Aluminum Alloys," *Journal of The Electrochemical Society*, vol. 155, no. 1, p. C1, 2008.

[8] C. Dong, Y. Ji, X. Wei, A. Xu, D. Chen, N. Li, D. Kong, X. Luo, K. Xiao, and X. Li, "Integrated computation of corrosion: Modelling, simulation and applications," *Corrosion Communications*, vol. 2, pp. 8–23, June 2021.

[9] E. L. Rooy, "Introduction to Aluminum and Aluminum Alloys," in *Properties and Selection: Nonferrous Alloys and Special-Purpose Materials*, vol. 2, ASM International, Jan. 1990.

[10] N. Birbilis and R. G. Buchheit, "Electrochemical Characteristics of Intermetallic Phases in Aluminum Alloys," *Journal of The Electrochemical Society*, vol. 152, no. 4, p. B140, 2005.

[11] R. Ambat, A. J. Davenport, G. M. Scamans, and A. Afseth, "Effect of iron-containing intermetallic particles on the corrosion behaviour of aluminium," *Corrosion Science*, vol. 48, pp. 3455–3471, Nov. 2006.

[12] Y. Liu, G. Z. Meng, and Y. F. Cheng, "Electronic structure and pitting behavior of 3003 aluminum alloy passivated under various conditions," *Electrochimica Acta*, vol. 54, pp. 4155–4163, July 2009.

[13] A. Laferrere, N. Parson, X. Zhou, and G. Thompson, "Effect of microstructure on the corrosion behaviour of extruded heat exchanger aluminium alloys," *Surface and Interface Analysis*, vol. 45, no. 10, pp. 1597–1603, 2013.

[14] G. M. Scamans, N. Birbilis, and R. G. Buchheit, "Corrosion of aluminum and its alloys," *Shreir's Corrosion*, pp. 1974–2010, Dec. 2010. Publisher: Elsevier.

[15] S. Y. Yu, W. E. O'Grady, D. E. Ramaker, and P. M. Natishan, "Chloride Ingress into Aluminum Prior to Pitting Corrosion An Investigation by XANES and XPS," *Journal of The Electrochemical Society*, vol. 147, p. 2952, Aug. 2000. Publisher: IOP Publishing.

[16] A. Kolics, J. Polkinghorne, A. Thomas, and A. Wieckowski, "Sorption of Sulfate and Chloride Anions on a Well-Characterized Al 2024 Electrode," *Chemistry of Materials*, vol. 10, no. 3, pp. 812–824, 1998.

[17] E. McCafferty, "Sequence of steps in the pitting of aluminum by chloride ions," *Corrosion Science*, vol. 45, pp. 1421–1438, July 2003.

[18] Z. Szklarska-Smialowska, "Pitting corrosion of aluminum," *Corrosion Science*, vol. 41, pp. 1743–1767, Aug. 1999.

[19] Y. J. Li and L. Arnberg, "Quantitative study on the precipitation behavior of dispersoids in DC-cast AA3003 alloy during heating and homogenization," *Acta Materialia*, vol. 51, pp. 3415–3428, July 2003.

[20] A. L. Dons, "The Alstruc homogenization model for industrial aluminum alloys," *Journal of Light Metals*, vol. 1, pp. 133–149, May 2001.

[21] W. D. Callister and D. G. Rethwisch, *Materials science and engineering: an introduction.* Wiley, 10 ed., 2018. OCLC: 992798798.

[22] H. J. McQueen, S. Spigarelli, M. E. Kassner, and E. Evangelista, "Extrusion," in *Hot Deformation and Processing of Aluminum Alloys*, pp. 461–522, CRC Press, 2011.

[23] X. Zhou, G. E. Thompson, and G. M. Scamans, "The influence of surface treatment on filiform corrosion resistance of painted aluminium alloy sheet," *Corrosion Science*, vol. 45, pp. 1767–1777, Aug. 2003.

[24] G. M. Scamans, A. Afseth, G. E. Thompson, and X. R. Zhou, "Ultra-Fine Grain Sized Mechanically Alloyed Surface Layers on Aluminium Alloys," *Materials Science Forum*, vol. 396-402, pp. 1461–1466, July 2002.

[25] J. L. Murray and A. J. McAlister, "The Al-Si (Aluminum-Silicon) system," *Bulletin of Alloy Phase Diagrams*, vol. 5, pp. 74–84, Feb. 1984.

[26] H. Leth-Olsen, J. H. Nordlien, and K. Nisancioglu, "Filiform corrosion of aluminium sheet. iii. microstructure of reactive surfaces," *Corrosion Science*, vol. 40, pp. 2051–2063, Dec. 1998.

[27] M. Fishkis and J. C. Lin, "Formation and evolution of a subsurface layer in a metalworking process," *Wear*, vol. 206, pp. 156–170, May 1997.

[28] J. T. B. Gundersen, A. Aytaç, S. Ono, J. H. Nordlien, and K. Nişancıoğlu, "Effect of trace elements on electrochemical properties and corrosion of aluminium alloy AA3102," *Corrosion Science*, vol. 46, pp. 265–283, Feb. 2004.

[29] B. Graver, A. T. J. van Helvoort, and K. Nisancioglu, "Effect of heat treatment on anodic activation of aluminium by trace element indium," *Corrosion Science*, vol. 52, pp. 3774–3781, Nov. 2010.

[30] Anawati, M. P. Halvorsen, and K. Nisancioglu, "Activation of Aluminum by Small Alloying Additions of Bismuth," *Journal of The Electrochemical Society*, vol. 159, p. C211, Feb. 2012. Publisher: IOP Publishing.

[31] Y. W. Keuong, J. H. Nordlien, S. Ono, and K. Nisancioglu, "Electrochemical Activation of Aluminum by Trace Element Lead," *Journal of The Electrochemical Society*, vol. 150, no. 11, p. B547, 2003.

[32] Y. Yu, Ø. Sævik, J. Nordlien, and K. Nisancioglu, "Effect of annealing temperature on anodic activation of rolled AA8006 aluminum alloy by trace element lead," *Journal of the Electrochemical Society*, vol. 152, no. 9, pp. B327–B333, 2005.

[33] Allan Blackman and Lawrie Gahan, *Aylward and Findlay's SI Chemical Data*. Wiley, 7 ed., 2013.

[34] A. J. McAlister, "The Al-Pb (Aluminum-Lead) system," *Bulletin of Alloy Phase Diagrams*, vol. 5, pp. 69–73, Feb. 1984.

[35] A. McAlister and D. Kahan, "The Al-Sn (Aluminum-Tin) System," *Bulletin of Alloy Phase Diagrams*, vol. 4, no. 4, pp. 410–414, 1983.

[36] J. L. Murray, "The Al-In (Aluminum-Indium) system," *Bulletin of Alloy Phase Diagrams*, vol. 4, pp. 271–278, Nov. 1983.

[37] J. L. Murray, "The Al-Ga (Aluminum-Gallium) system," *Bulletin of Alloy Phase Diagrams*, vol. 4, pp. 183–190, Sept. 1983.

[38] C. J. Coombes, "The melting of small particles of lead and indium," *Journal of Physics F: Metal Physics*, vol. 2, pp. 441–449, May 1972. Publisher: IOP Publishing.

[39] H. W. Sheng, "Superheating and melting-point depression of Pb nanoparticles embedded in Al matrices," *Philosophical Magazine Letters*, vol. 73, pp. 179–186, Apr. 1996.

[40] J. Tan, J. C. Walmsley, B. Holme, H. Nordmark, and K. Nisancioglu, "Surface segregation of tin by heat treatment of dilute aluminium–tin alloys," *Corrosion Science*, vol. 68, pp. 204–213, Mar. 2013.

[41] J. C. Walmsley, Ø. Sævik, B. Graver, R. H. Mathiesen, Y. Yu, and K. Nisancioglu, "Nature of Segregated Lead on Electrochemically Active AlPb Model Alloy," *Journal of The Electrochemical Society*, vol. 154, p. C28, Nov. 2006. Publisher: IOP Publishing.

[42] Ø. Sævik, Y. Yu, J. H. Nordlien, and K. Nisancioglu, "Characterization of Lead Enrichment on Electrochemically Active AlPb Model Alloy," *Journal of The Electrochemical Society*, vol. 152, p. B334, July 2005. Publisher: IOP Publishing.

[43] Anawati, B. Graver, H. Nordmark, Z. Zhao, G. S. Frankel, J. C. Walmsley, and K. Nisancioglu, "Multilayer Corrosion of Aluminum Activated by Lead," *Journal of The Electrochemical Society*, vol. 157, p. C313, Aug. 2010. Publisher: IOP Publishing.

[44] H. Gabrisch, U. Dahmen, and E. Johnson, "In Situ Observations of the Interaction of Liquid Lead Inclusions with Grain Boundaries in Aluminum," *Microscopy and Microanalysis: The Official Journal of Microscopy Society of America, Microbeam Analysis Society, Microscopical Society of Canada*, vol. 4, pp. 286–293, May 1998.

[45] B. Graver, A. van Helvoort, J. C. Walmsley, and K. Nisancioglu, "Surface Segregation of Indium by Heat Treatment of Aluminium," *Materials Science Forum*, vol. 519-521, pp. 673–678, July 2006.

[46] Juan Tan, *Dissertation, NTNU 2011:241.* PhD thesis, NTNU, Trondheim, Norway, Sept. 2011.

[47] E. Senel and K. Nisancioglu, "Anodic activation of aluminium containing small amounts of gallium and tin," *Corrosion Science*, vol. 88, pp. 280–290, Nov. 2014.

[48] K. Kurt, S. Diplas, J. C. Walmsley, and K. Nisancioglu, "Effect of Trace Elements Lead and Tin on Anodic Activation of AA8006 Aluminum Sheet," *Journal of The Electrochemical Society*, vol. 160, p. C542, Sept. 2013. Publisher: IOP Publishing.

[49] E. Senel and K. Nisancioglu, "Effect of small concentrations of gallium and lead on anodic activation of aluminium in chloride solution," *Corrosion Science*, vol. 131, pp. 330–339, Feb. 2018.

[50] K. Nisancioglu, "Significance of Trace Element Segregation in Corrosion of Aluminum Alloys," in *Proceedings of the 12th International Conference on Aluminium Alloys,*, (Yokohama, Japan), pp. 1455–1462, Sept. 2010.

[51] K. Oldham, J. Myland, and A. Bond, *Electrochemical Science and Technology: Fundamentals and Applications.* John Wiley & Sons, Dec. 2011.

[52] L. I. Stephens, S. C. Perry, S. M. Gateman, R. Lacasse, R. Schulz, and J. Mauzeroll, "Development of a Model for Experimental Data Treatment of Diffusion and Activation Limited Polarization Curves for Magnesium and Steel Alloys," *Journal of The Electrochemical Society*, vol. 164, no. 11, pp. E3576–E3582, 2017.

[53] H. J. Flitt and D. P. Schweinsberg, "A guide to polarisation curve interpretation: deconstruction of experimental curves typical of the Fe/H2O/H+/O2 corrosion system," *Corrosion Science*, vol. 47, pp. 2125–2156, Sept. 2005.

[54] S. Trasatti, "Work function, electronegativity, and electrochemical behaviour of metals: III. Electrolytic hydrogen evolution in acid solutions," *Journal of Electroanalytical Chemistry and Interfacial Electrochemistry*, vol. 39, pp. 163–184, Sept. 1972.

[55] X. Gong, C. Dong, J. Xu, L. Wang, and X. Li, "Machine learning assistance for electrochemical curve simulation of corrosion and its application," *Materials and Corrosion*, vol. 71, no. 3, pp. 474–484, 2020.

[56] M. Aghaaminiha, R. Mehrani, M. Colahan, B. Brown, M. Singer, S. Nesic, S. M. Vargas, and S. Sharma, "Machine learning modeling of time-dependent corrosion rates of carbon steel in presence of corrosion inhibitors," *Corrosion Science*, vol. 193, p. 109904, Dec. 2021.

[57] Y. Diao, L. Yan, and K. Gao, "Improvement of the machine learning-based corrosion rate prediction model through the optimization of input features," *Materials & Design*, vol. 198, p. 109326, Jan. 2021.

[58] ASTM Standard D1141, (2021), "Standard Practice for Preparation of Substitute Ocean Water," 2021.

[59] Gamry Instruments, "Potentiodynamic Scan / Cyclic Polarization," 2019. https://www.gamry.com/application-notes/corrosion-coatings/potentiodynamic-cyclic-polarization.

[60] Halvor Frøhaug Willumsen, "Reconstructing polarisation curves of aluminium alloys by using machine learning," tech. rep., NTNU, Trondheim, Dec. 2021.

[61] F. Pedregosa, G. Varoquaux, A. Gramfort, V. Michel, B. Thirion, O. Grisel, M. Blondel, P. Prettenhofer, R. Weiss, V. Dubourg, J. Vanderplas, A. Passos, and D. Cournapeau, "Scikit-learn: Machine Learning in Python," *MACHINE LEARNING IN PYTHON*, p. 6, Oct. 2011.

[62] Kathrine Storli, "Mechanistic investigation of the pretreatment of AA6060 with varying Ni and Cu content," Master's thesis, NTNU, Trondheim, June 2022.

[63] M. Seo, H. Habazaki, and T. Nakayama, "Effect of Pb-underpotential deposition on anodic dissolution and passivation of pure Fe and Fe-Ni alloys in acidic perchlorate solution," *Journal of Solid State Electrochemistry*, vol. 20, pp. 3133–3142, Nov. 2016.

[64] W. M. Carroll, M. Murphy, and C. B. Breslin, "The corrosion/dissolution behaviour of aluminium in solutions containing both chloride and fluoride ions," *Corrosion Science*, vol. 34, pp. 1495–1507, Sept. 1993.

Appendix A

Experimental Polarisation Curves

The raw polarisation curves used to train the machine learning model are presented in this appendix. All polarisation curves were collected with a sweep rate of 0.1 mV/s in SWAAT solution. The electrolyte were purged for 5 minutes with nitrogen gas to remove dissolved oxygen before the start the first polarisation scan for each sample.

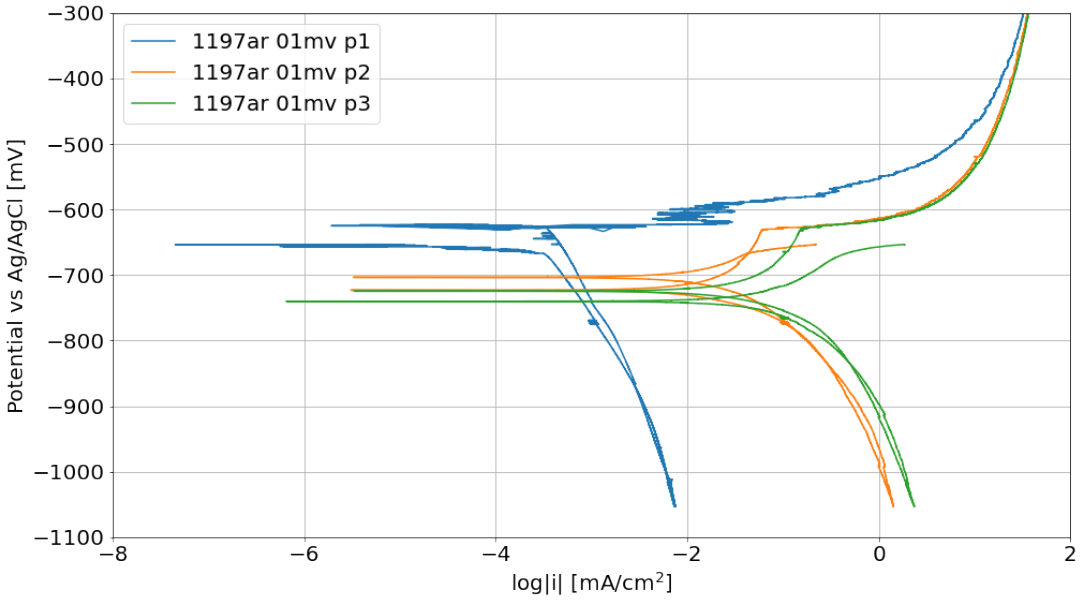

Figure A.1: Polarisation curves for the 1197ar specimen.

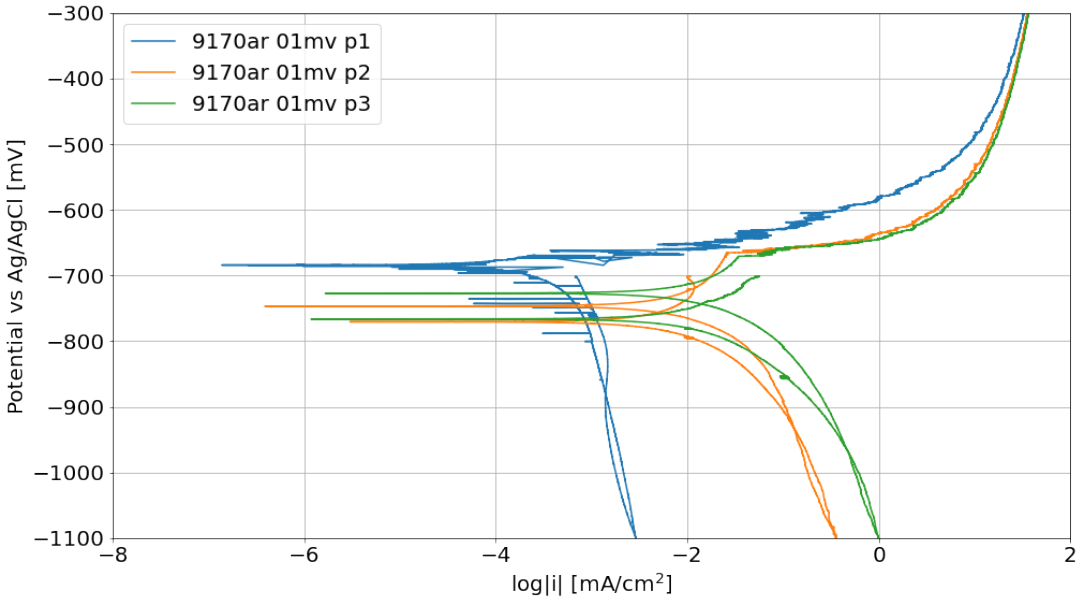

Figure A.2: Polarisation curves for the 9170ar specimen.

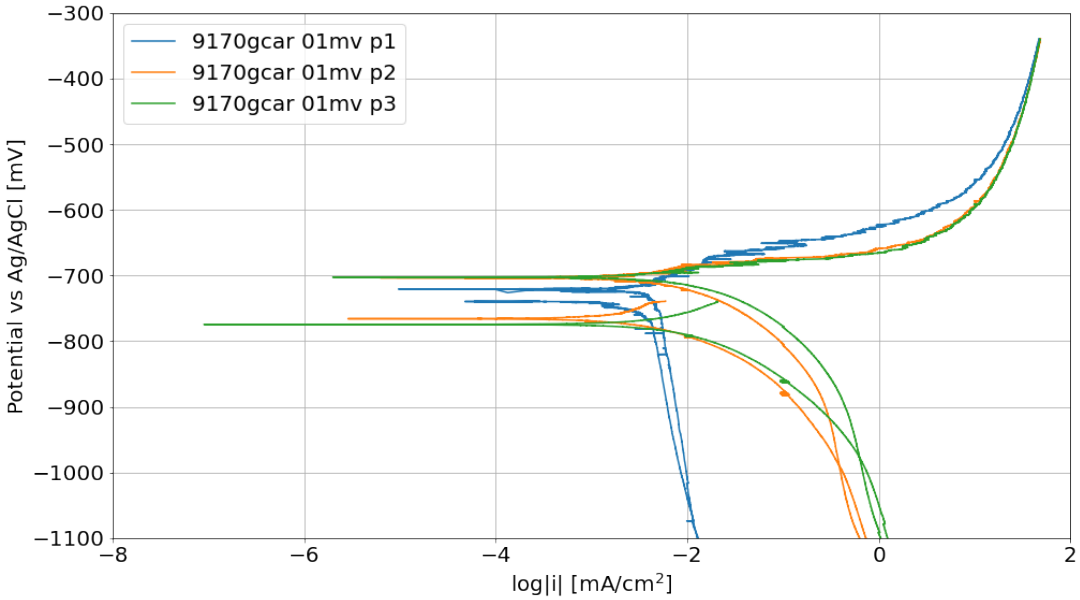

Figure A.3: Polarisation curves for the 9170gcar specimen.

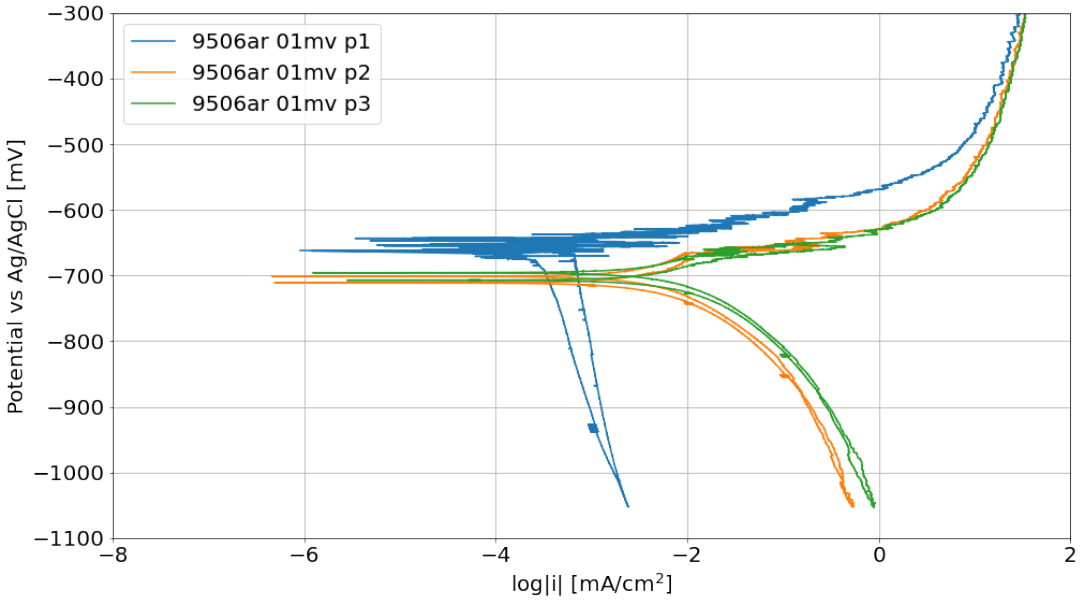

Figure A.4: Polarisation curves for the 9506ar specimen.

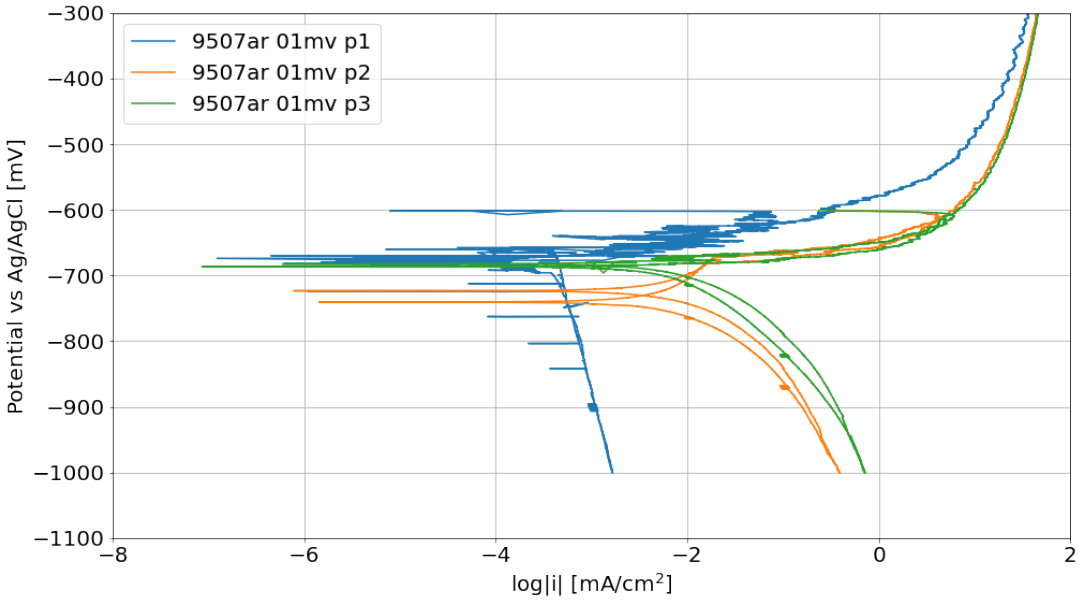

Figure A.5: Polarisation curves for the 9507ar specimen.

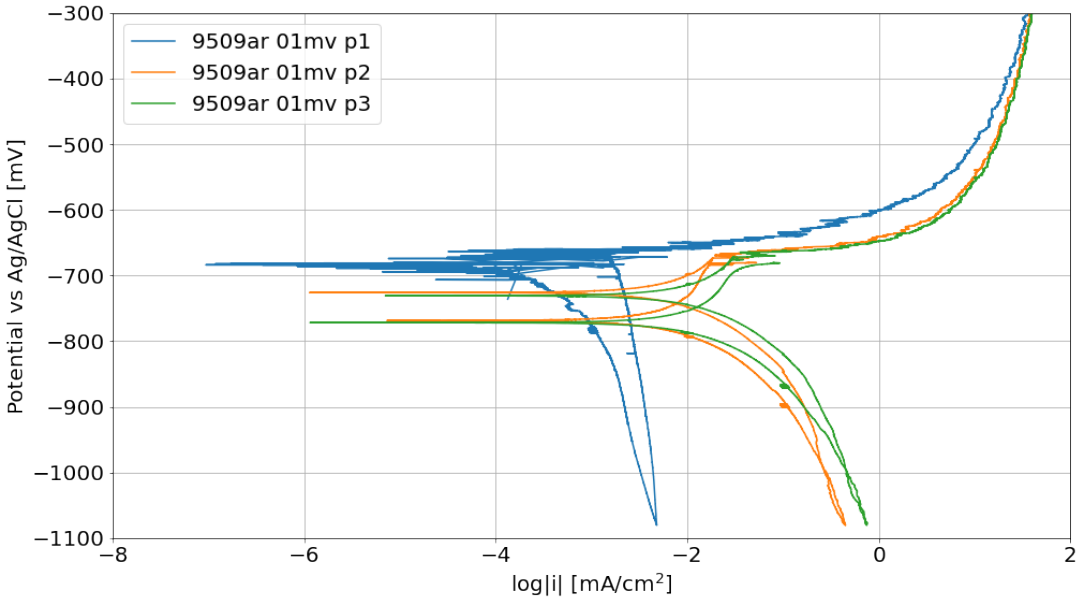

Figure A.6: Polarisation curves for the 9509ar specimen.

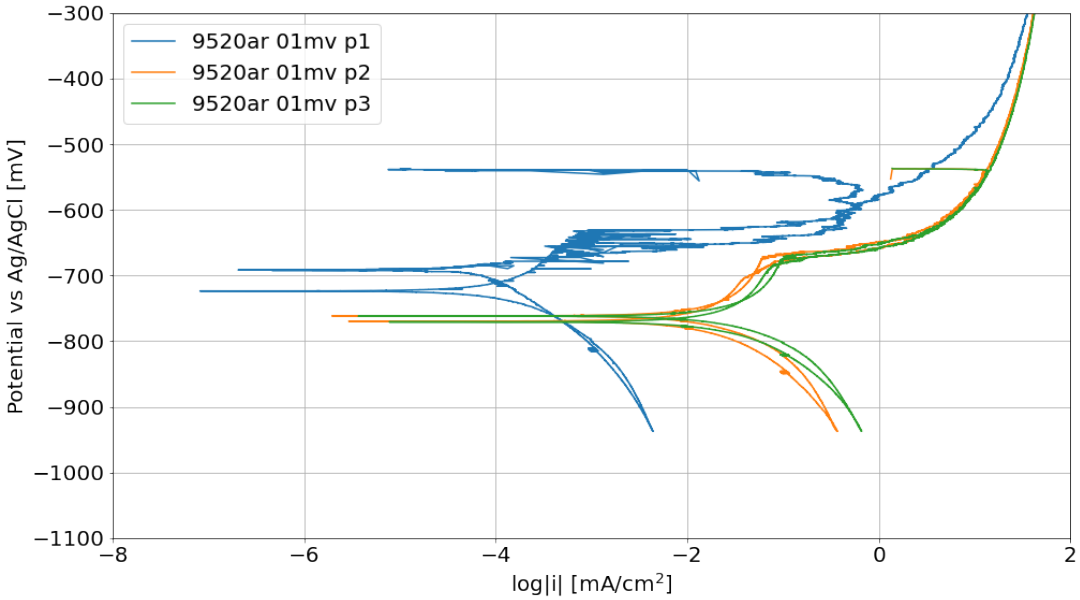

Figure A.7: Polarisation curves for the 9520ar specimen.

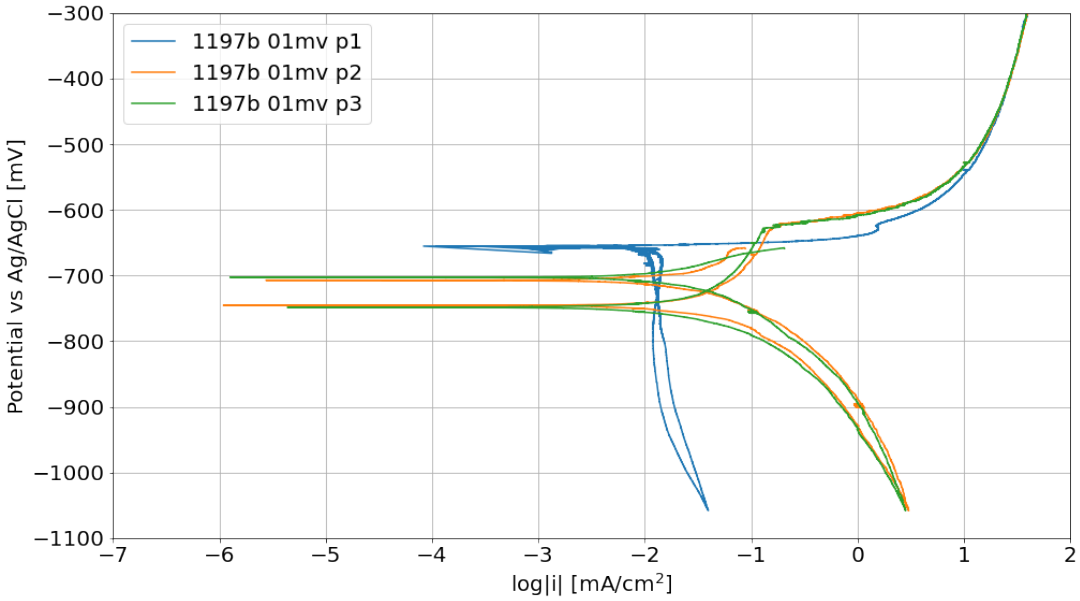

Figure A.8: Polarisation curves for the 1197b specimen.

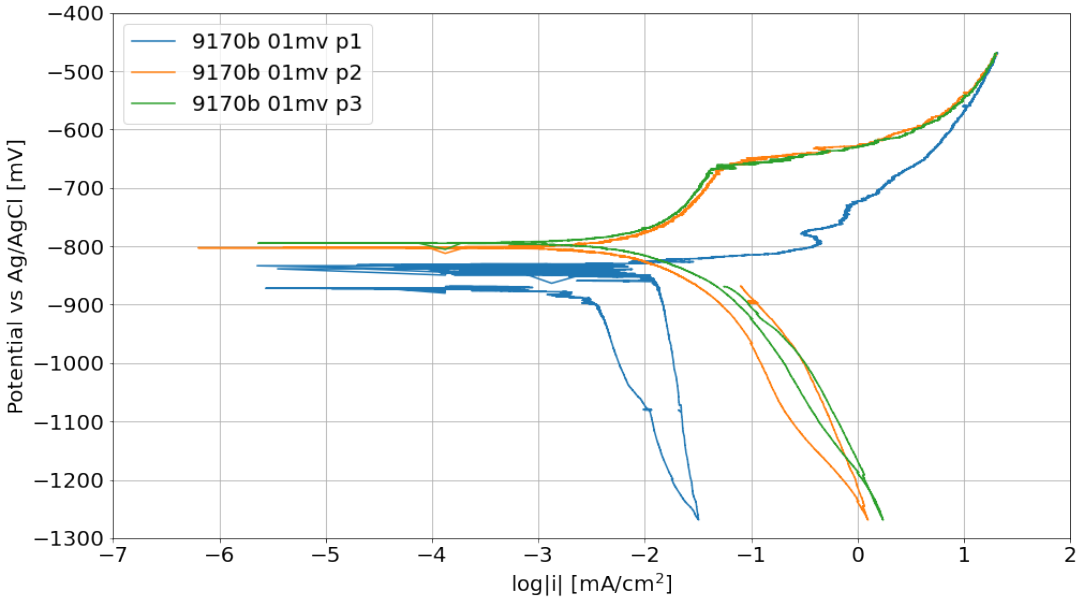

Figure A.9: Polarisation curves for the 9170b specimen.

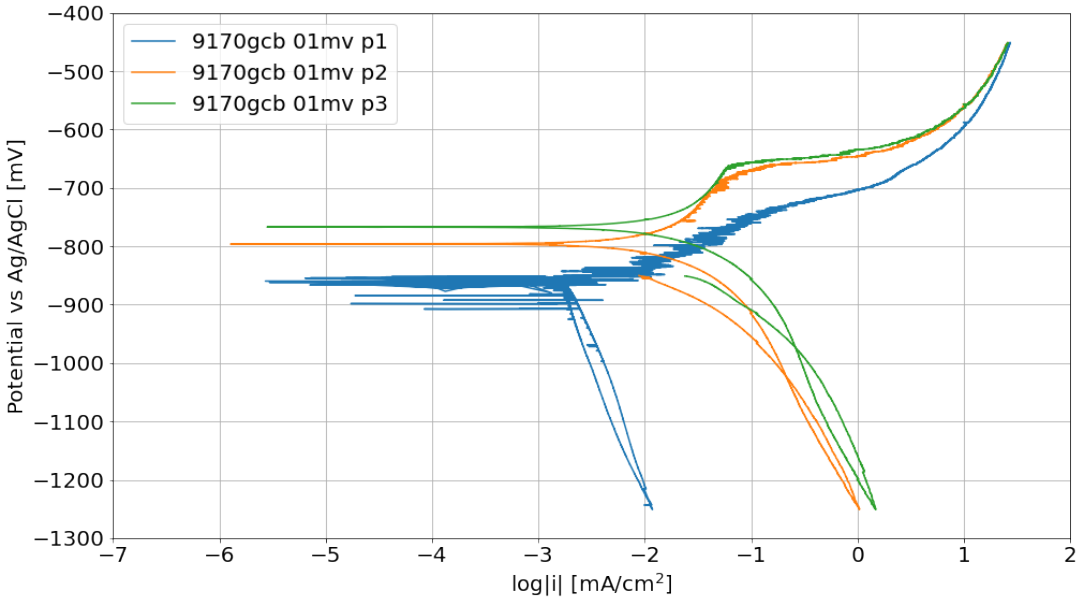

Figure A.10: Polarisation curves for the 9170gcb specimen.

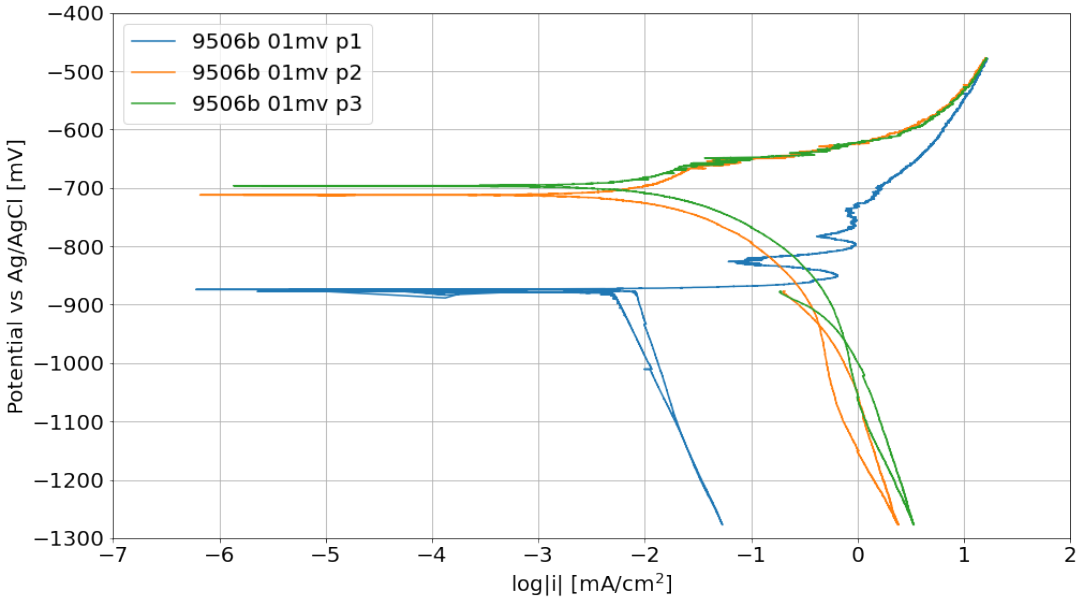

Figure A.11: Polarisation curves for the 9506b specimen.

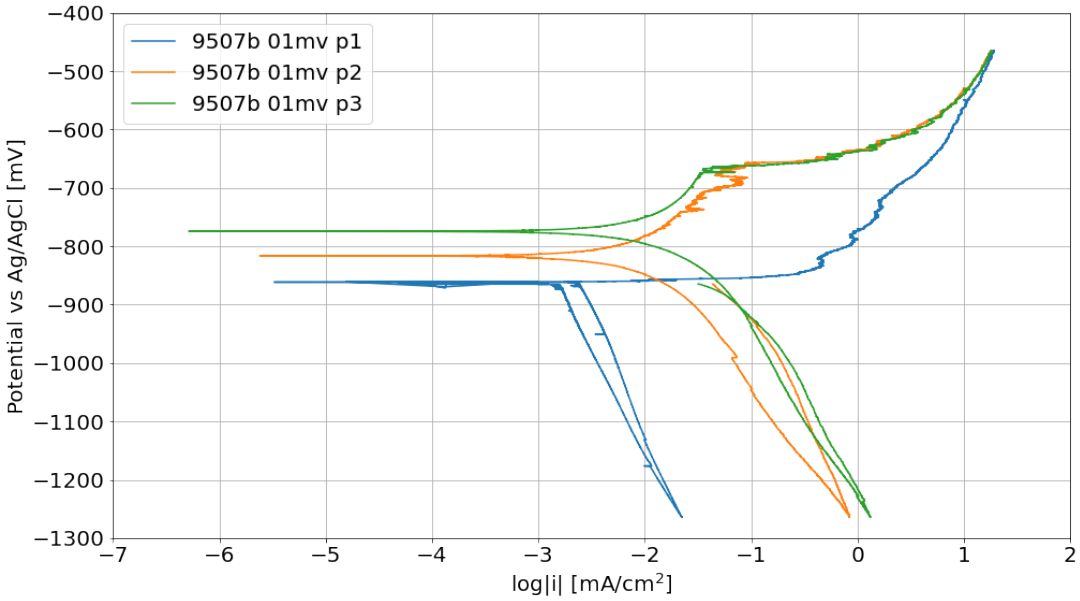

Figure A.12: Polarisation curves for the 9507b specimen.

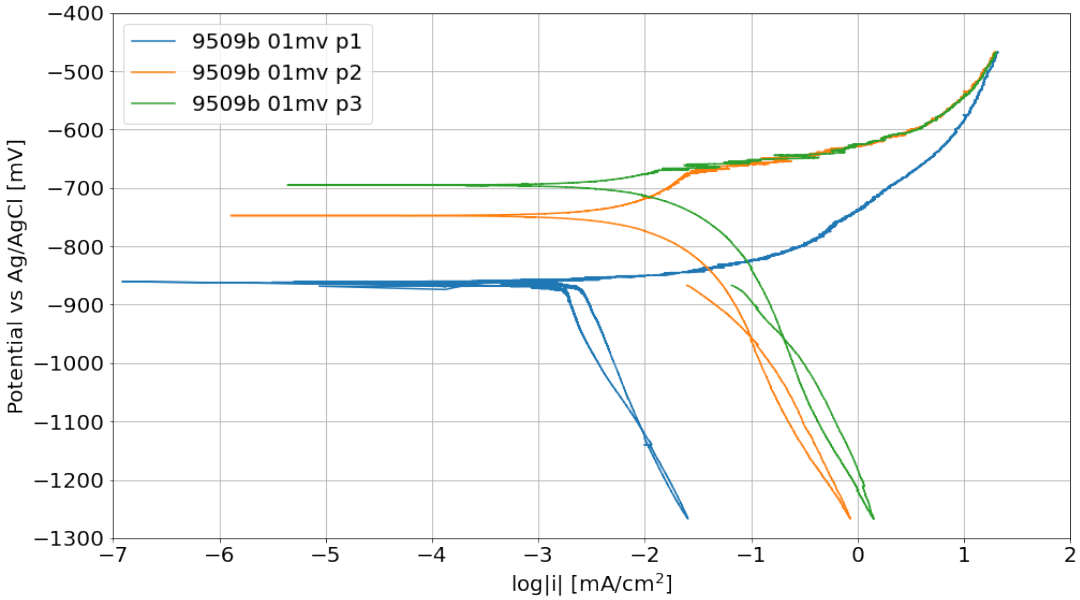

Figure A.13: Polarisation curves for the 9509b specimen.

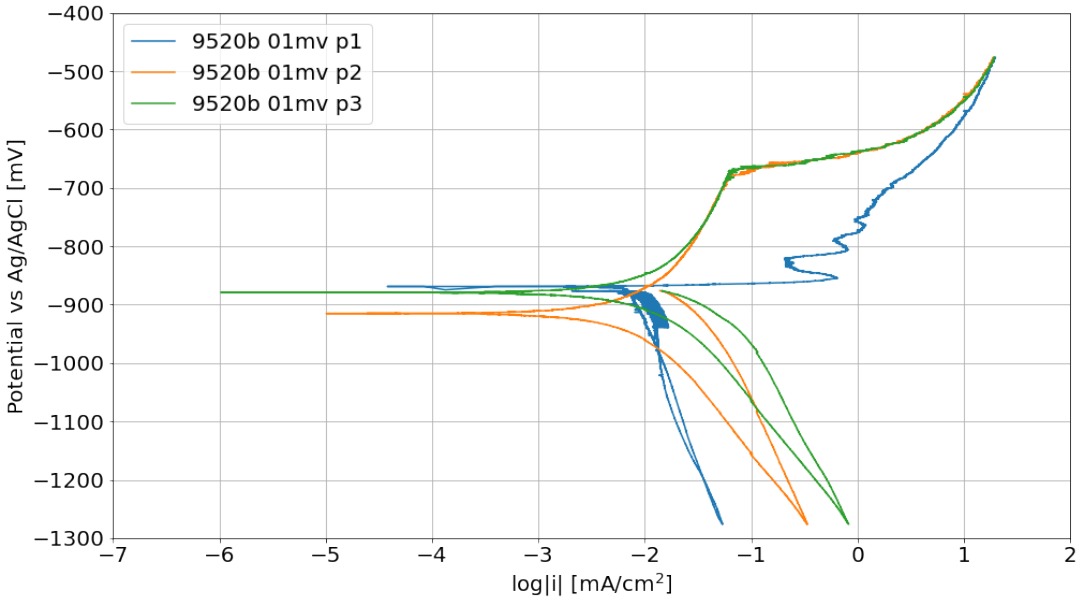

Figure A.14: Polarisation curves for the 9520b specimen.

Appendix B

GD-OES

Chemical depth profiles for alloys not presented in chapter 4 are presented in this appendix.

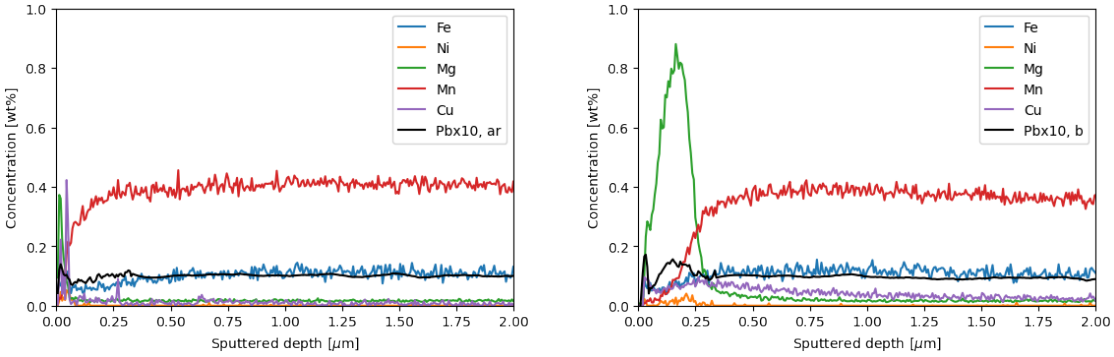

(a) **(b)**

Figure B.1: GD-OES elemental depth profiles for the **(a)** as-extruded and **(b)** as-brazed samples of the 9170 alloy.

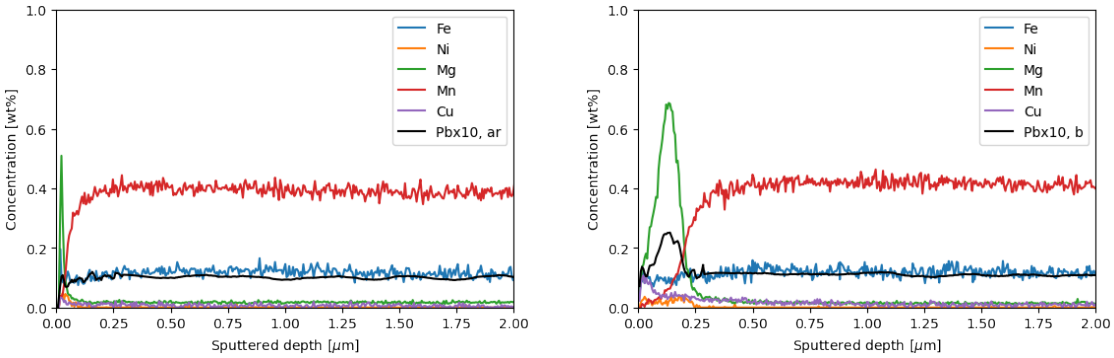

(a) **(b)**

Figure B.2: GD-OES elemental depth profiles for the **(a)** as-extruded and **(b)** as-brazed samples of the 9170gc alloy.

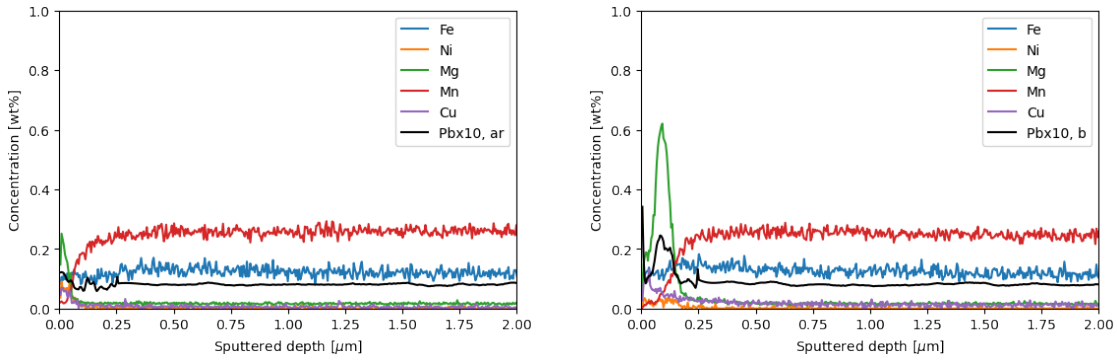

(a) **(b)**

Figure B.3: GD-OES elemental depth profiles for the **(a)** as-extruded and **(b)** as-brazed samples of the 9507 alloy.

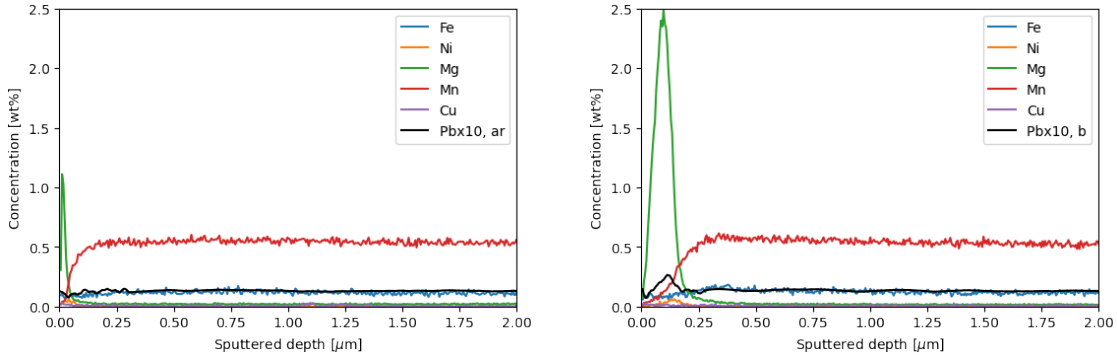

(a) **(b)**

Figure B.4: GD-OES elemental depth profiles for the **(a)** as-extruded and **(b)** as-brazed samples of the 9509 alloy.

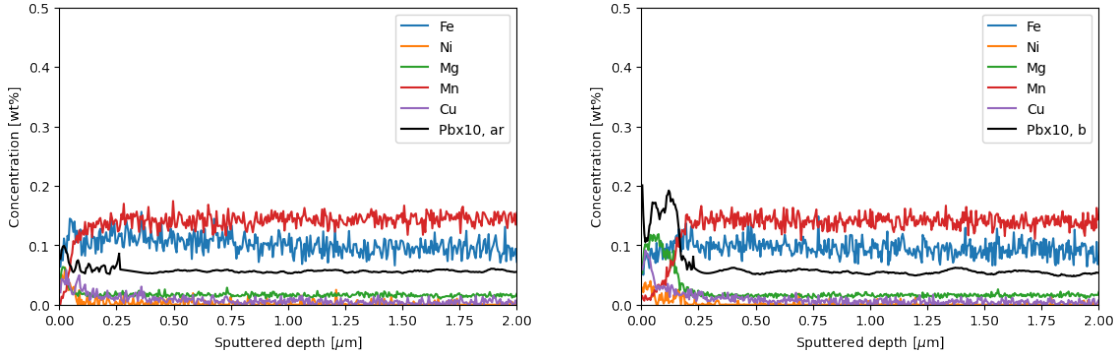

(a) **(b)**

Figure B.5: GD-OES elemental depth profiles for the **(a)** as-extruded and **(b)** as-brazed samples of the 9520 alloy.

Appendix C

Code

[2]:
```
import pandas as pd
import numpy as np
import matplotlib.pyplot as plt
import random

from sklearn.ensemble import RandomForestRegressor
from sklearn.model_selection import train_test_split
from sklearn.metrics import mean_absolute_error as mae
```

[ ]:
```
def testingFunction(E, content, first=False):
    title=['Si', 'Fe', 'Mn', 'Cu']
    mat=content*np.ones((len(E), 1))
    df=pd.DataFrame(mat, columns=title)
    if(first):
        firstTest=np.ones(len(E))
    else:
        firstTest=np.zeros(len(E))
    df['First?']=firstTest
    df['E']=E
    features=['Si', 'Fe', 'Mn', 'Cu', 'First?', 'E']
    df
    x=df.loc[:, features].values
    return x
```

[ ]:
```
def newLabFormatter(prefix, content, rounds=3):
    title=['Si', 'Fe', 'Mn', 'Cu']
    x=np.zeros(1)
    y=np.zeros(1)
    sec=0
    for j in range(rounds):
        filename=prefix+str(j+1)+'.DTA'
        E,i=np.loadtxt(filename, unpack=True, usecols=(0,1),␣
 ↪skiprows=1, delimiter=',')
```

```
        if(j==0):
            first=np.ones(len(E))
        else:
            sec+=len(E)
        x=np.concatenate((x,E))
        y=np.concatenate((y,i))
    second=np.zeros(sec)
    firstSecond=np.concatenate((first, second))
    a=np.ones((len(x)-1,1))
    matrix=content*a
    df=pd.DataFrame(matrix, columns=title)
    df['First?']=firstSecond
    df['E']=x[1:]
    df['i']=y[1:]*1000/A
    features=['Si', 'Fe', 'Mn', 'Cu', 'First?', 'E']
    xRet=df.loc[:,features].values
    yRet=df.loc[:,'i'].values
    return xRet, yRet
```

[4]:
```
def picker(x,y,array, n):
    r=random.sample(array, n)
    print(r)
    count=0
    for element in rr:
        key=r[count][:5]
        path=element+' 01mv p'
        l,m=newLabFormatter(path, master[key])
        x=np.concatenate((x,l))
        y=np.concatenate((y,m))
        count+=1
    return x,y
```

[2]:
```
#contentAlloy = array([Si,  Fe    Mn    Cu ])

content1197=np.array([0.15, 0.18, 0.15, 0.44])

content9108=np.array([0.12, 0.20, 0.7, 0.000001])

content9170=np.array([0.06, 0.10, 0.43, 0.000001])

content9170gc=np.array([0.044, 0.096, 0.43, 0.003])

content9506=np.array([0.26, 0.16, 0.58, 0.002])

content9507=np.array([0.07, 0.13, 0.29, 0.001])

content9509=np.array([0.07, 0.10, 0.56, 0.000001])
```

```
content9510=np.array([0.18, 0.17, 0.6, 0.001])

content9520=np.array([0.07, 0.09, 0.16, 0.000001])

A=(0.885/2)**(2)*np.pi
master={'1197b':content1197, '9108b':content9108, '9170b':content9170,␣
 ↪'9170g':content9170gc, '9506b':content9506, '9507b':content9507,␣
 ↪'9509b':content9509, '9510b':content9510, '9520b':content9520}
```

[5]:
```
a,b=newLabFormatter('9108b r1 01mv p', content9108, rounds=3)
brazed=['1197b','9170b','9170gcb','9506b','9507b','9509b','9510b␣
 ↪r1','9520b']
x,y=picker(a,b,brazed, 6)
```

[7]:
```
X_train, X_test, y_train, y_test = train_test_split(x, y,␣
 ↪random_state=0, train_size=0.9)
reg = RandomForestRegressor(n_estimators=500, random_state = 1234,␣
 ↪n_jobs=-1)
reg.fit(X_train, y_train)
```

[9]:
```
importance = reg.feature_importances_
features=['Si', 'Fe', 'Mn', 'Cu', 'First?', 'E']
for i in range(len(importance)):
    print(features[i]+': '+str(round(100*importance[i],5))+'%')
print(reg.score(X_test, y_test))
```

[10]:
```
####Testing of the predictive accuracy when the 1197b alloy was left␣
 ↪out of the training data

E_p3, i_p3=np.loadtxt('1197b 01mv p3.DTA', unpack=True, usecols=(0,1),␣
 ↪skiprows=1, delimiter=',')
E_p1, i_p1=np.loadtxt('1197b 01mv p1.DTA', unpack=True, usecols=(0,1),␣
 ↪skiprows=1, delimiter=',')

iPred_p3=reg.predict(testingFunction(E_p3, content1197, first=False))
iPred_p1=reg.predict(testingFunction(E_p1, content1197, first=True))

plt.scatter(np.log10(np.abs(iPred_p3)), E_p3*1000, label='Predicted␣
 ↪curve 1197b p3', color='black')
plt.scatter(np.log10(np.abs(iPred_p1)), E_p1*1000, label='Predicted␣
 ↪curve 1197b p1', color='black', marker='x')

plt.plot(np.log10(np.abs(i_p3*1000/A)), E_p3*1000, label='Experimental␣
 ↪data 1197b p3', color='red')
plt.plot(np.log10(np.abs(i_p1*1000/A)), E_p1*1000, label='Experimental␣
 ↪data 1197b p1', color='blue')
```

```
####Control plot, used for controlling overfitting. Appropriate alloy␣
 ↪for controlling is chosen based on alloy composition
EControl, iControl=np.loadtxt(filename of selected alloy, unpack=True,␣
 ↪usecols=(0,1), skiprows=1, delimiter=',')
plt.plot(np.log10(np.abs(iControl*1000/A)), EControl*1000,␣
 ↪label='Experimental data control plot', color='green')


###Plot aestethics
plt.grid()
plt.xlabel(r'log|i| [mA/cm$^2$]')
plt.ylabel('Potential vs Ag/AgCl [mV]')
plt.xlim(-6, 2)
plt.ylim(-1300, -300)
plt.legend()
plt.show()
```

[11]:
```
print('R^2 1197b p3: ',reg.score(testingFunction(E_p3, content1197),␣
 ↪i_p3*1000/A))
print('R^2 1197b p1: ',reg.score(testingFunction(E_p1, content1197),␣
 ↪i_p1*1000/A))
print('MAE 1197b p3: ',mae(np.abs(i_p3*1000/A), np.abs(iPred_p3)))
print('MAE 1197b p1: ',mae(np.abs(i_p1*1000/A), np.abs(iPred_p1)))
```

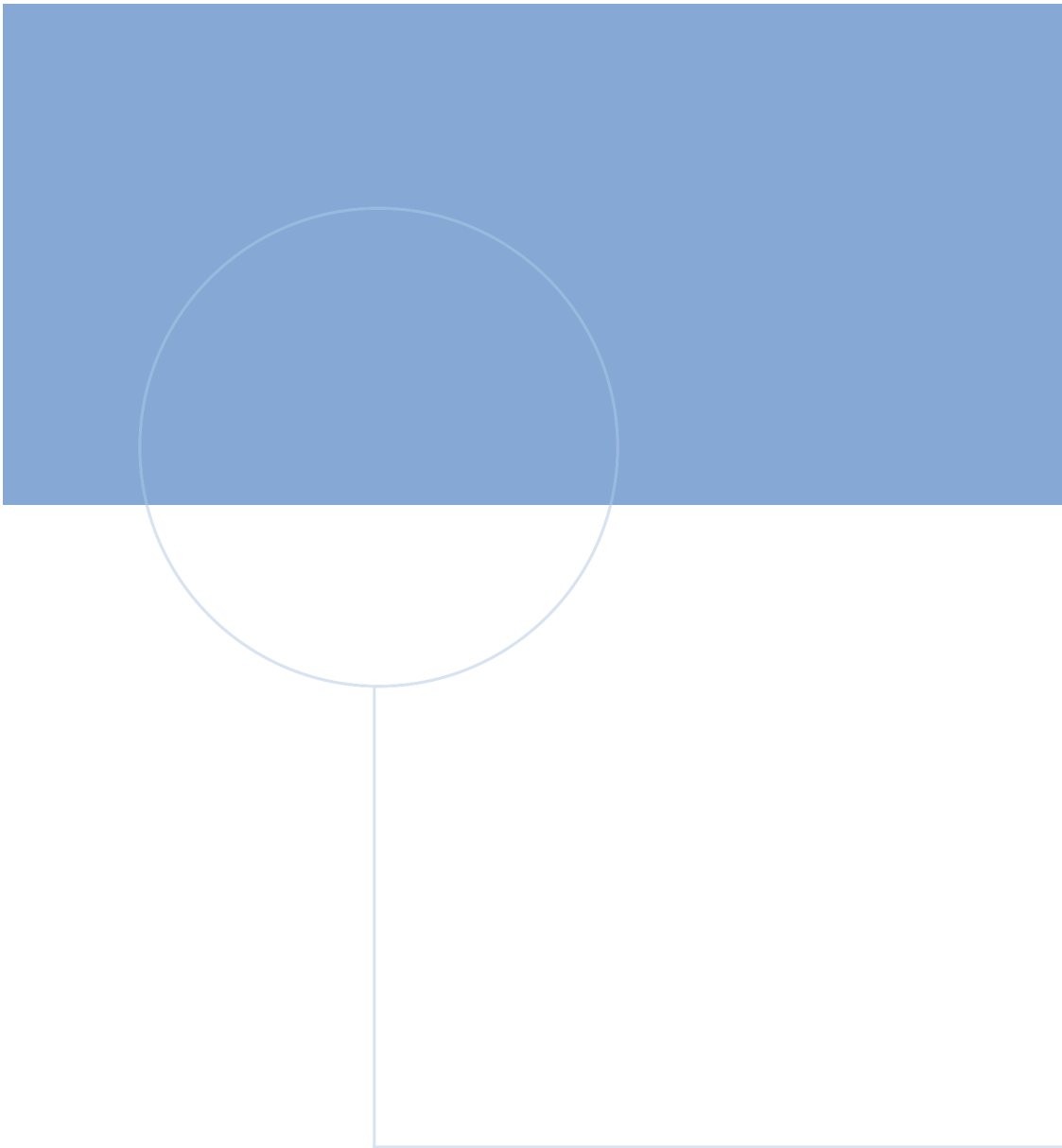

NTNU

Norwegian University of
Science and Technology